

A Wide and Deep Exploration of Radio Galaxies with Subaru HSC (WERGS). II. Physical Properties Derived from the SED Fitting with Optical, Infrared, and Radio Data

著者	Yoshiki Toba, Takuji Yamashita, Tohru Nagao, Wei-Hao Wang, Yoshihiro Ueda, Kohei Ichikawa, Toshihiro Kawaguchi, Masayuki Akiyama, Bau-Ching Hsieh, Masaru Kajisawa, Chien-Hsiu Lee, Yoshiki Matsuoka, Akatoki Noboriguchi, Masafusa Onoue, Malte Schramm, Masayuki Tanaka, Yutaka Komiyama
journal or publication title	The Astrophysical Journal Supplement Series
volume	243
number	1
page range	15
year	2019-07-17
URL	http://hdl.handle.net/10097/00128253

doi: 10.3847/1538-4365/ab238d



A Wide and Deep Exploration of Radio Galaxies with Subaru HSC (WERGS). II. Physical Properties Derived from the SED Fitting with Optical, Infrared, and Radio Data

Yoshiki Toba^{1,2,3} , Takuji Yamashita^{3,4} , Tohru Nagao³ , Wei-Hao Wang² , Yoshihiro Ueda¹ , Kohei Ichikawa^{5,6} ,
Toshihiro Kawaguchi⁷, Masayuki Akiyama⁵ , Bau-Ching Hsieh² , Masaru Kajisawa^{3,8} , Chien-Hsiu Lee⁹ ,
Yoshiki Matsuoka³, Akatoki Noboriguchi⁸ , Masafusa Onoue¹⁰ , Malte Schramm⁴, Masayuki Tanaka^{4,11} , and
Yutaka Komiyama^{4,11}

¹ Department of Astronomy, Kyoto University, Kitashirakawa-Oiwake-cho, Sakyo-ku, Kyoto 606-8502, Japan; toba@kusastro.kyoto-u.ac.jp

² Academia Sinica Institute of Astronomy and Astrophysics, 11F of Astronomy-Mathematics Building, AS/NTU, No.1, Section 4, Roosevelt Road, Taipei 10617, Taiwan

³ Research Center for Space and Cosmic Evolution, Ehime University, 2-5 Bunkyo-cho, Matsuyama, Ehime 790-8577, Japan

⁴ National Astronomical Observatory of Japan, 2-21-1 Osawa, Mitaka, Tokyo 181-8588, Japan

⁵ Astronomical Institute, Tohoku University, 6-3 Aramaki, Aoba-ku, Sendai, Miyagi 980-8578, Japan

⁶ Frontier Research Institute for Interdisciplinary Sciences, Tohoku University, 6-3 Aramaki, Aoba-ku, Sendai, Miyagi 980-8578, Japan

⁷ Department of Economics, Management and Information Science, Onomichi City University, Hisayamada 1600-2, Onomichi, Hiroshima 722-8506, Japan

⁸ Graduate School of Science and Engineering, Ehime University, Bunkyo-cho, Matsuyama, Ehime 790-8577, Japan

⁹ National Optical Astronomy Observatory, 950 N Cherry Ave., Tucson, AZ 85719, USA

¹⁰ Max-Planck-Institut für Astronomie, Königstuhl 17, D-69117 Heidelberg, Germany

¹¹ Department of Astronomy, School of Science, Graduate University for Advanced Studies (SOKENDAI), 2-21-1 Osawa, Mitaka, Tokyo 181-8588, Japan

Received 2019 January 14; revised 2019 May 2; accepted 2019 May 3; published 2019 July 17

Abstract

We present physical properties of radio galaxies (RGs) with $f_{1.4\text{ GHz}} > 1\text{ mJy}$ discovered by Subaru Hyper Suprime-Cam (HSC) and Very Large Array Faint Images of the Radio Sky at Twenty-Centimeters (FIRST) survey. For 1056 FIRST RGs at $0 < z \leq 1.7$ with HSC counterparts in about 100 deg^2 , we compiled multi-wavelength data of optical, near-infrared (IR), mid-IR, far-IR, and radio (150 MHz). We derived their color excess ($E(B - V)_*$), stellar mass, star formation rate (SFR), IR luminosity, the ratio of IR and radio luminosity (q_{IR}), and radio spectral index (α_{radio}) that are derived from the spectral energy distribution (SED) fitting with CIGALE. We also estimated Eddington ratio based on stellar mass and integration of the best-fit SEDs of active galactic nucleus (AGN) component. We found that $E(B - V)_*$, SFR, and IR luminosity clearly depend on redshift while stellar mass, q_{IR} , and α_{radio} do not significantly depend on redshift. Since optically faint ($i_{\text{AB}} \geq 21.3$) RGs that are newly discovered by our RG survey tend to be high redshift, they tend to not only have a large dust extinction and low stellar mass but also have high SFR and AGN luminosity, high IR luminosity, and high Eddington ratio compared with optically bright ones. The physical properties of a fraction of RGs in our sample seem to differ from a classical view of RGs with massive stellar mass, low SFR, and low Eddington ratio, demonstrating that our RG survey with HSC and FIRST provides us curious RGs among entire RG population.

Key words: catalogs – infrared: galaxies – methods: observational – methods: statistical – radio continuum: galaxies

Supporting material: machine-readable tables

1. Introduction

In the last decade, observational and theoretical works have reported that feedback from radio active galactic nuclei (AGNs) harbored in radio galaxies (RGs) and radio-loud quasars can play an important role in the formation and evolution of galaxies (e.g., Croton et al. 2006; Fabian 2012). Mechanical injection of energy from RGs provides an impact on the gas reservoirs in galaxies and galaxy clusters (Morganti et al. 2013). Such AGN feedback could regulate star formation (SF) and even the growth of supermassive black holes (SMBHs) in galaxies. Therefore, it is important to investigate the physical properties related to SF and AGN activity for RGs as a function of redshift in order to understand a full picture of the formation and evolution of galaxies.

A multi-wavelength data set of optical and infrared (IR) for RGs is crucial for studying their physical properties, such as stellar mass, AGN/SF activity, and star formation rate (SFR). For example, a combination of National Radio Astronomy Observatory Very Large Array (VLA) Sky Survey (NVSS; Condon 1989)

or the VLA Faint Images of the Radio Sky at Twenty-Centimeters survey (FIRST; Becker et al. 1995), and the Sloan Digital Sky Survey (SDSS; York et al. 2000) provided a larger number of RGs with optical counterparts in the local universe (Ivezić et al. 2002; Best et al. 2005; Helfand et al. 2015), allowing us a statistical investigation of those “optically bright” RGs with $r < 22.2\text{ mag}$ at redshift $z < 0.5$. These objects have been well studied in terms of UV/optical properties (e.g., de Ruiter et al. 2015), morphologies (e.g., Liske et al. 2015; Aniyon & Thorat 2017; Lukic et al. 2018), mid-IR (MIR) properties (e.g., Gürkan et al. 2014), and far-IR (FIR) properties (e.g., Gürkan et al. 2015, 2018), as well as black hole (BH) mass and its accretion rate (e.g., Best & Heckman 2012). Almost all of the optically bright local RGs have elliptical hosts with stellar mass of $> 10^{10.5} M_{\odot}$ and SFR of $< 10 M_{\odot} \text{ yr}^{-1}$ (Best & Heckman 2012). Only a small fraction of the local RGs has relatively small stellar mass with moderate star-forming activities (Smolčić 2009; Best & Heckman 2012).

At the high- z universe ($z > 1$), known RGs are powerful or radio-luminous ($L_{\text{radio}} \gtrsim 10^{26} \text{ W Hz}^{-1}$, corresponding to $> 0.1\text{ mJy}$). The powerful high- z RGs are dominated by the

evolved stellar populations with a stellar mass of $10^{11-12} M_{\odot}$ (e.g., Rocca-Volmerange et al. 2004; Seymour et al. 2007; Casey et al. 2009). The IR luminosity (L_{IR}) of those powerful high- z RGs often exceed $10^{12} L_{\odot}$ that is classified as ultraluminous IR galaxy (ULIRG; Sanders & Mirabel 1996). They also show the evidence of high SFR and high BH accretion rate through IR and submillimeter observations (e.g., Chapman et al. 2010; Magnelli et al. 2010; Seymour et al. 2012; Drouart et al. 2014; Bonzini et al. 2015). On the other hand, Falkendal et al. (2019) investigated the SFR of those powerful high- z RGs based on multi-wavelength SEDs, taking into account their synchrotron emission. They reported that their SFRs are indeed lower than those of a main sequence of galaxies, suggesting an importance of multi-wavelength analysis for RGs.

Deep radio and optical observations enable us to find much fainter RGs (see Padovani 2016, and references therein) and to provide a comprehensive understanding by connecting RGs between local and high- z universe. Delvecchio et al. (2018) investigated RGs in the VLA-COSMOS field (Smolčić et al. 2017b) based on a multi-wavelength data set (Laigle et al. 2016; Smolčić et al. 2017a). They found that an average BH mass accretion rate, represented by a ratio of bolometric luminosity to stellar mass, increases with increasing redshift up to $z \sim 4$. They also reported that this trend is similar to the fact that a fraction of star-forming host galaxies also increase with increasing redshift. Although their statistical experiment was performed with a relatively small area ($\sim 2 \text{ deg}^2$), a wide-field survey with deep radio and optical facilities enables us to find a large number of “optically faint” RGs, providing us a laboratory to investigate their evolution in more high resolutions in redshifts and luminosities.

Recently, Yamashita et al. (2018, Paper I) performed a systematic search for RGs and quasars as a project called “The Wide and Deep Exploration of Radio Galaxies with Subaru HSC (WERGS).” They reported the result of optical identifications of radio sources detected by FIRST with the Hyper Suprime-Cam (HSC; Miyazaki et al. 2012, 2018) (see also, Furusawa et al. 2018; Kawanomoto et al. 2018; Komiyama et al. 2018 Subaru Strategic Program survey (HSC-SSP); Aihara et al. 2018a). By cross-matching the final data release of the FIRST survey (Helfand et al. 2015) with HSC S16A data (Aihara et al. 2018b), they found 3579 optical counterparts of FIRST sources in a 154 deg^2 of a HSC-SSP Wide field (see Section 2.1). Their radio flux densities at 1.4 GHz (20 cm) are above 1 mJy, while about 60% of them are optically faint ones with $i \geq 21.3 \text{ mag}$ that are undetected by the SDSS, allowing us to explore a new parameter space, i.e., optically faint bright radio sources. Plenty of RG and quasar samples also gives us an opportunity to discover a specially rare population, for example, a radio galaxy (RG) at high redshift (T. Yamashita et al. 2019, in preparation) and extremely radio-loud quasars (K. Ichikawa et al. 2019, in preparation).

This is the second in a series of papers from the WERGS project, in which we report the physical properties of radio-loud galaxies at $0 < z \leq 1.7$ with i -band magnitude between 18 and 26 that are derived from the spectral energy distribution (SED) fitting of multi-wavelength data. In this paper, we follow the same definition of RGs and quasars as adopted in Yamashita et al. (2018). But we removed stellar objects, i.e., radio-loud quasars that are optically unresolved objects based

on optical morphology (see Yamashita et al. 2018), and focus only on RGs that have optically resolved morphologies.

The structure of this paper is as follows. Section 2 describes the sample selection of RGs, the multi-wavelength data set, and our SED modeling. In Section 3, we report the result of SED fitting and the derived physical quantities of RGs detected by the HSC and FIRST. In Section 4, we discuss a possible selection bias, an uncertainty of our SED fitting, and BH mass accretion rate for our sample. We summarize this work in Section 5. All information about our RG sample, such as coordinates, multi-band photometry, and derived physical quantities, is available as a catalog (see Appendix A). We also provide best-fit SED templates of those RGs (see Appendix B). Throughout this paper, the adopted cosmology is a flat universe with $H_0 = 70 \text{ km s}^{-1} \text{ Mpc}^{-1}$, $\Omega_M = 0.27$, and $\Omega_{\Lambda} = 0.73$, which are same as those adopted in Yamashita et al. (2018). Unless otherwise noted, all magnitudes refer to the AB system.

2. Data and Analysis

2.1. Sample Selection

Figure 1 shows a flow chart of our sample selection process. The original sample was drawn from 3579 RGs and quasars in Yamashita et al. (2018), who used the HSC-SSP and FIRST data. The HSC-SSP is an ongoing optical imaging survey with five broadband filters (g -, r -, i -, z -, and y -band) and four narrowband filters (see Aihara et al. 2018a; Bosch et al. 2018; Coupon et al. 2018; Huang et al. 2018). This survey consists of three layers, Wide, Deep, and UltraDeep, and this work uses S16A Wide-layer data¹² obtained from 2014 March to 2016 January, providing a forced photometry of g -, r -, i -, z -, and y -band with a 5σ limiting magnitude of 26.8, 26.4, 26.4, 25.5, and 24.7, respectively (Aihara et al. 2018b). The HSC-SSP Wide-layer covers six fields (XMM-LSS, GAMA09H, WIDE12H, GAMA15H, HECTOMAP, and VVDS; see Table 1 in Yamashita et al. (2018) for detailed coordinates of each field). The typical seeing is about $0''.6$ in the i -band, and the astrometric uncertainty is about 40 mas in root mean square (rms). Taking into account the photometric and astrometric flags, Yamashita et al. (2018) eventually extracted 23,795,523 HSC objects in the 154 deg^2 for cross-matching with FIRST (see Section 2.1 in Yamashita et al. 2018 for more detail).

The FIRST project completed radio imaging survey at 1.4 GHz with a spatial resolution of $5''.4$ (Becker et al. 1995; White et al. 1997) covering $10,575 \text{ deg}^2$, which is completely overlapping with the survey footprint of the HSC-SSP Wide-layer, and the final release catalog of FIRST (Helfand et al. 2015) is publicly available. Before cross-matching with the HSC, Yamashita et al. (2018) made a flux-limited FIRST sample with flux density at 1.4 GHz greater than 1.0 mJy. Taking into account a flag that tells a source is a spurious detection near a bright source, Yamashita et al. (2018) eventually extracted 7072 FIRST objects in the 154 deg^2 for the cross-matching with the HSC (see Section 2.2 in Yamashita et al. 2018 for more detail). By cross-matching the HSC S16A Wide-layer catalog and FIRST final data release catalog with a search radius of $1''$, 3579 objects (including RGs and radio-loud quasars) were selected (see Section 3 in Yamashita et al. 2018 for more detail).

¹² The S16A data (Wide, Deep, and UltraDeep) is available in 2019 as a public data release 2 (Aihara et al. 2019). Although Yamashita et al. (2018) used UltraDeep data in addition to Wide data, this work focuses only on Wide data.

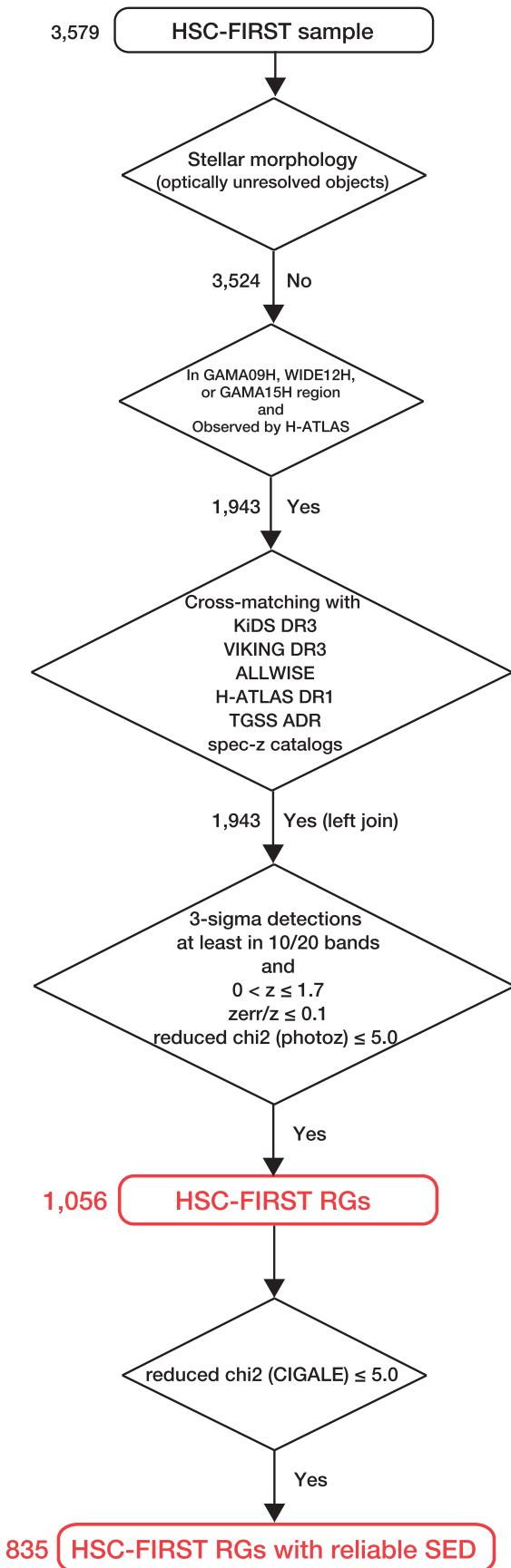


Figure 1. Flow chart of the sample selection process.

Before compiling multi-wavelength data, we made a parent RG sample. First, we removed 55 stellar objects (i.e., radio-loud quasars) based on optical morphological information (see Yamashita et al. 2018). For $3579 - 55 = 3524$ RGs, we then narrowed down the sample to 2118 objects in three fields with a total area of $\sim 94.7 \text{ deg}^2$ (GAMA09H, WIDE12H, and GAMA15H) where multi-wavelength data are available. We then removed 175 objects that are not covered by FIR observation (see Section 2.1.4), which yielded 1943 RGs. The sky distribution of those 1943 RGs is shown in Figure 2. For those objects, we then compiled the multi-wavelength data from u -band, near-IR (NIR), MIR, FIR, and radio data, as well as spectroscopic or photometric redshift. After removing 897 objects with photometric data less than 10, and unreliable photometric redshift and/or photometric redshift greater than 1.7 (see Section 2.1.6), we finally selected $1943 - 897 = 1056$ objects (hereafter “HSC-FIRST RGs”) with multi-wavelength data and reliable redshift in this work.

2.1.1. u -band Data

The u -band data were taken from the Kilo-Degree Survey (KiDS; de Jong et al. 2013), which is an ESO public survey carried out with the VLT Survey Telescope (VST) and OmegaCAM camera (Kuijken 2011). We used the Data Release (DR) 3 (de Jong et al. 2017), which consists of 48,736,590 sources with a limiting magnitude of 24.3 mag (5σ in a $2''$ aperture) in u -band. The typical full width at half maximum (FWHM) of point-spread function (PSF) for u -band detected point sources is about $1''$.¹³ Before the cross-matching, we extracted 42,252,797 sources with `FLAG_U = 0` to ensure clean photometry in u -band (see de Jong et al. 2015, 2017 for more detail).

2.1.2. Near-IR Data

We compiled NIR data from the VISTA Kilo-degree Infrared Galaxy Survey (VIKING; Arnaboldi et al. 2007) DR3¹⁴ that includes 73,747,647 sources in $\sim 1000 \text{ deg}^2$ with NIR taken by the VISTA InfraRed Camera (VIRCAM; Dalton et al. 2006). We used J -, H -, and K_s -band with a median 10σ (Vega) magnitude limit of 20.1, 19.0, and 18.6 mag, respectively. Objects with a PSF FWHM of $< 1''/2$ was observed in VIKING. Before the cross-matching, we selected 63,028,265 objects with `primary_source=1` and (`jpperrbits < 256` or `hpperrbits < 256` or `kspperrbits < 256`) to ensure clean photometry for uniquely detected objects (see also Toba et al. 2015; Noboriguchi et al. 2019).

2.1.3. Mid-IR Data

The MIR data were taken from *Wide-field Infrared Survey Explorer* (WISE; Wright et al. 2010). We utilized W1 ($3.4 \mu\text{m}$), W2 ($4.6 \mu\text{m}$), W3 ($12 \mu\text{m}$), and W4 ($22 \mu\text{m}$) data in ALLWISE (Cutri et al. 2014) that consists of 747,634,026 sources. The 5σ detection limits¹⁵ in W1, W2, W3, and W4 band are approximately 0.054, 0.071, 0.73, and 5 mJy, respectively. The angular resolutions in W1, W2, W3, and W4 band are $6''.1$, $6''.4$, $6''.5$, and $12''.0$, respectively. We extracted

¹³ http://kids.strw.leidenuniv.nl/DR3/catalog_table.php

¹⁴ <http://eso.org/rm/api/v1/public/releaseDescriptions/107>

¹⁵ http://wise2.ipac.caltech.edu/docs/release/allwise/expsup/sec2_3a.html

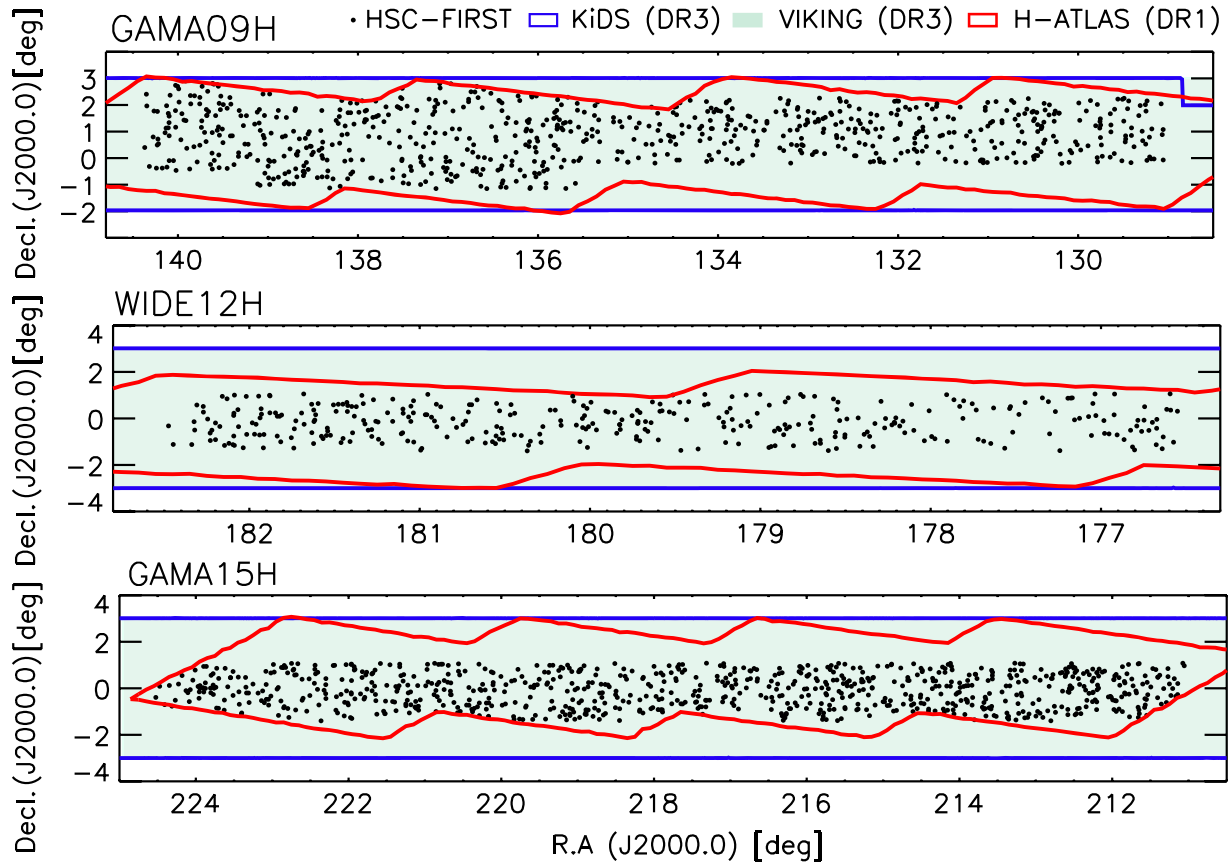


Figure 2. Spatial distribution (J2000.0) of 1943 HSC-FIRST radio galaxies (black points) in GAMA09H (top), WIDE12H (middle), and GAMA15H (bottom) field. Blue, green, and red squares represent survey footprint of KiDS, VIKING, and H-ATLAS, respectively. Those regions are completely covered by ALLWISE and TGSS. There are 754, 344, and 845 HSC-FIRST objects in the GAMA09H, WIDE12H, and GAMA15H, respectively.

741,753,366 sources with ($w1sat = 0$ and $w1cc_map = 0$) or ($w2sat = 0$ and $w2cc_map = 0$) or ($w3sat = 0$ and $w3cc_map = 0$), or ($w4sat = 0$ and $w4cc_map = 0$) in the ALLWISE catalog (Cutri et al. 2014), to have secure photometry at either band (see the Explanatory Supplement to the ALLWISE Data Release Products¹⁶ for more detail).

2.1.4. Far-IR Data

We also used FIR data that were provided by a project of the *Herschel Space Observatory* (Pilbratt et al. 2010) Astrophysical Terahertz Large Area Survey (H-ATLAS; Eales et al. 2010; Bourne et al. 2016). The data were taken with the Photoconductor Array Camera and Spectrometer (PACS; Poglitsch et al. 2010) at 100 and 160 μm and with the Spectral and Photometric Imaging REceiver instrument (SPIRE; Griffin et al. 2010) at 250, 350, and 500 μm . The typical PSF FWHMs of 100, 160, 250, 350, and 500 μm are $11''.4$, $13''.7$, $17''.8$, $24''.0$, and $35''.2$, respectively. We used H-ATLAS DR1 (Valiante et al. 2016) containing 120,230 sources in the galaxy and mass assembly (GAMA) fields. The 1σ noise for source detection (that includes confusion and instrumental noise) is 44, 49, 7.4, 9.4, and 10.2 mJy at 100, 160, 250, 350, and 500 μm , respectively (Valiante et al. 2016).

2.1.5. Ancillary Radio Data

The radio data were taken from observations with the Giant Metrewave Radio Telescope (GMRT; Swarup 1991). We used

continuum flux density at 150 MHz (~ 1.99 m) provided by the Tata Institute of Fundamental Research (TIFR) GMRT Sky Survey (TGSS) alternative data release (ADR; Intema et al. 2017), which includes 623,604 radio sources in 36,900 deg^2 . The median rms noise of sources is $3.5 \text{ mJy beam}^{-1}$, with a spatial resolution of about $25''$.

2.1.6. Cross-identification of Multi-band Catalogs

We then cross-identified those catalogs (KiDS, VIKING, ALLWISE, H-ATLAS, and TGSS) with HSC-FIRST RGs.¹⁷ By using a search radius of $1''$ for KiDS and VIKING, $3''$ for ALLWISE, $10''$ for H-ATLAS, and $20''$ for TGSS, 1051 (54.1%), 1564 (80.5%), 1482 (76.3%), 257 (13.2%), and 471 (24.2%) objects were cross-identified by KiDS, VIKING, ALLWISE, H-ATLAS, and TGSS, respectively. We note that 3/1051 ($\sim 0.3\%$) and 2/471 ($\sim 0.4\%$) objects have two candidates of counterpart for VIKING and TGSS sources, respectively, within the search radius. We choose the nearest object as a counterpart for such cases. For cross-matching with other catalogs (KiDS, ALLWISE, and H-ATLAS), one-to-one identification was realized. The matches by chance coincidence are estimated by generating mock catalogs with random positions, in the same manner as Yamashita et al. (2018). We generated mock catalogs of KiDS, VIKING, ALLWISE, H-ATLAS, and TGSS data where source position in each catalog is shifted from the original one to $\pm 1^\circ$ or $\pm 2^\circ$ along the

¹⁶ <http://wise2.ipac.caltech.edu/docs/release/allwise/expsup/index.html>

¹⁷ We always use right ascension and decl. in the HSC catalog as coordinates of HSC-FIRST objects.

right assignation direction (see Yamashita et al. 2018 for more detail). We then cross-identified HSC–FIRST RGs with those mock catalogs with the exactly same search radii. We found that the chance coincidence of cross-matching with the KiDS, VIKING, ALLWISE, H-ATLAS, and TGSS catalogs is about 5.0%, 1.9%, 3.4%, 9.3%, and 0.6%, respectively.

We also compiled photometric and spectroscopic redshift. For spectroscopic redshift, we utilized the SDSS DR12 (Alam et al. 2015), the GAMA project DR2 (Driver et al. 2011; Liske et al. 2015), and WiggleZ Dark Energy Survey project DR1 (Drinkwater et al. 2010). For photometric redshift, we employed a custom-designed Bayesian photometric redshift code (MIZUKI; Tanaka 2015) to estimate the photometric redshift (photo- z) of HSC–FIRST objects in the same manner as Yamashita et al. (2018), in which we used z_{best} as a photometric redshift (see also Tanaka et al. 2018). In order to perform an accurate SED fitting, we preferentially used spectroscopic redshift. For objects without spectroscopic redshift, we used their z_{best} if they have a reliable photometric redshift, i.e., $0 < z_{\text{best}} \leq 1.7$,¹⁸ $\sigma_{z_{\text{best}}}/z_{\text{best}} \leq 0.1$, and reduced χ^2 of $z_{\text{best}} \leq 5.0$. These criteria are optimized based on the comparison with spectroscopic redshift for the WERGS sample in Yamashita et al. (2018) (see also Tanaka et al. 2018). However, the influence of the above criteria on physical quantities derived from the SED fitting is still unclear, which will be discussed in Section 4.2.1. In addition to the above redshift (quality) cut, we extracted objects with $>3\sigma$ detection in at least 10 photometric bands among 20 photometric data ($u, g, r, i, z, y, J, H, K_s$ -band; 3.4, 4.6, 12, 22, 100, 160, 250, 350; 500 μm ; and 150 and 1400 MHz) to avoid an overfitting for our SED fitting method (see Section 2.2). Consequently, 1056 HSC–FIRST RGs with multi-band photometry and reliable redshift were left (see Figure 1). Among 1056 objects, the redshifts of 224, 44, and 3 objects were taken from the SDSS DR12, GAMA DR2, and WiggleZ DR1, respectively, while the redshifts of the remaining 785 objects were taken from MIZUKI. The HSC–FIRST RG catalog, which includes basic information such as redshift and multi-band photometry, is accessible through an online service. Format and column descriptions of the catalog are summarized in Table 3.

2.2. SED Modeling with CIGALE

We here employed CIGALE¹⁹ (Code Investigating GALaxy Emission; Burgarella et al. 2005; Noll et al. 2009; Boquien et al. 2019) in order to perform a detailed SED modeling in a self-consistent framework with considering the energy balance between the UV/optical and IR. In this code, we are able to handle many parameters, such as star formation history (SFH), single stellar population (SSP), attenuation law, AGN emission, dust emission, and radio synchrotron emission.

We assumed an SFH of two exponential decreasing SFR with different e-folding times (Ciesla et al. 2015, 2016). We adopted the stellar templates provided from Bruzual & Charlot (2003) assuming the initial mass function (IMF) in Chabrier (2003), and the standard default nebular emission model included in CIGALE (see Inoue 2011). Dust attenuation is modeled by using the Calzetti et al. (2000) law with color

excess ($E(B - V)_*$). We note that even if we employ the dust attenuation law of the Small Magellanic Cloud that would be applicable to dusty starburst galaxies, resultant physical properties are consistent with what we present in this work within error. The reprocessed IR emission of dust absorbed from UV/optical stellar emission is modeled assuming dust templates of Dale et al. (2014). For AGN emission, we also utilized models provided in Fritz et al. (2006), where we fixed some parameters that determine the density distribution of the dust within the torus to avoid a degeneracy of AGN templates in the same manner as Ciesla et al. (2015). We parameterized the ψ parameter (an angle between the AGN axis and the line of sight) that corresponds to a viewing angle of the torus. We also parameterize AGN fraction (f_{AGN}), which is the contribution of IR luminosity from AGN to the total IR luminosity (Ciesla et al. 2015). For radio synchrotron emission from either SFG or AGN, we parameterized a correlation coefficient between FIR and radio luminosity (q_{IR}) and the slope of power-law synchrotron emission (α_{radio}) (but see Sections 3.5.6 and 3.5.7). We define α_{radio} from the measured radio flux density at observed-frame frequencies at 150 MHz and 1.4 GHz, assuming a power-law radio spectrum of $f_\nu \propto \nu^{-\alpha_{\text{radio}}}$;

$$\alpha_{\text{radio}} = \frac{\log(F_{150 \text{ MHz}}/F_{1.4 \text{ GHz}})}{\log(\nu_{1.4 \text{ GHz}}/\nu_{150 \text{ MHz}})}. \quad (1)$$

This synchrotron emission is cut off at 100 μm ; that is, a default value adopted in CIGALE that would be optimized for normal star-forming galaxies. However, the synchrotron emission may contribute to fluxes/luminosities even at $<100 \mu\text{m}$, especially for radio-loud AGNs (e.g., Mason et al. 2012; Privon et al. 2012; Falkendal et al. 2019; Rakshit et al. 2019). In this work, we choose 30 μm as a cutoff wavelength of the synchrotron emission with a single power law, in the same manner as Lyu & Rieke (2018) (see also Pe'er 2014). We have confirmed that the choice of cutoff wavelength does not significantly affect the following results. Table 1 lists the detailed parameter ranges adopted in the SED fitting (see also Matsuoka et al. 2018; Chen et al. 2019; Toba et al. 2019). In addition to the energy balance between UV/optical and IR part, CIGALE takes into account the balance between IR and radio luminosity that is parameterized by q_{IR} , which are eventually an essential framework in CIGALE.

To find a best-fit SED and calculate physical properties and their uncertainties, CIGALE employed an analysis module so-called `pdf_analysis`. This module computes the likelihood (that corresponds to χ^2) for all the possible combinations of parameters and generates the probability distribution function (PDF) for each parameter and each object. But before computing the likelihood, the module scaled the models by a factor (α) to obtain physically meaningful values (so-called extensive physical properties) such as stellar masses and IR luminosities, where α can be derived as follows:

$$\alpha = \frac{\sum_i \frac{f_i m_i}{\sigma_i^2}}{\sum_i \frac{m_i^2}{\sigma_i^2}} + \frac{\sum_j \frac{f_j m_j}{\sigma_j^2}}{\sum_j \frac{m_j^2}{\sigma_j^2}}, \quad (2)$$

where f_i and m_i are the observed and model flux densities, f_j and m_j are the observed and model extensive physical properties, and σ is the corresponding uncertainties (see Equation (13) in Boquien et al. 2019). Finally, `pdf_analysis` computes the

¹⁸ Yamashita et al. (2018) reported that the HSC–SSP photo- z derived by MIZUKI could be secure at $z \leq 1.7$ based on comparison with spectroscopic redshift in COSMOS field (see Section 5.1.2 in Yamashita et al. 2018 for more detail).

¹⁹ <https://cigale.lam.fr/2018/11/07/version-2018-0/>

Table 1
Parameter Ranges Used in the SED Fitting with CIGALE

Parameter	Value
Double exp. SFH	
τ_{main} [Myr]	1000, 3000, 4000, 6000
τ_{burst} [Myr]	3, 5, 8, 15, 80
f_{burst}	0.001, 0.1, 0.3
age [Myr]	1000, 4000, 6000, 8000, 10000
SSP (Bruzual & Charlot 2003)	
IMF	Chabrier (2003)
Metallicity	0.02
Dust attenuation (Calzetti et al. 2000)	
$E(B - V)_*$	0.01, 0.1, 0.15, 0.2, 0.25, 0.3, 0.35, 0.4, 0.45, 0.5, 0.55, 0.6, 0.8, 1.0
AGN emission (Fritz et al. 2006)	
$R_{\text{max}}/R_{\text{min}}$	60
$\tau_{9,7}$	6.0
β	-0.50
γ	0.0
θ	100.0
ψ	0.001, 60.100, 89.990
f_{AGN}	0.1, 0.5, 0.9
Dust emission (Dale et al. 2014)	
IR power-law slope (α_{dust})	0.0625, 0.2500, 1.0000, 2.0000
Radio synchrotron emission	
$L_{\text{FIR}}/L_{\text{radio}}$ coefficient (q_{IR})	00.01, 0.1, 0.3, 0.5, 1.0, 2.5
spectral index (α_{radio})	0.5, 0.7, 0.9, 1.1, 1.3

probability-weighted mean and standard deviation that correspond to resultant value and its uncertainty for each parameter, in which α is considered as a free parameter. This approach is fully valid as far as one compares models built from the same set of parameters (see Section 4.3 in Boquien et al. 2019 for full explanation of this module) (see also, Salim et al. 2007).

Under the parameter setting described in Table 1, we fit the stellar, AGN, SF, and radio components to at most 20 photometric points ($u, g, r, i, z, y, J, H, K_s$ -band, and 3.4, 4.6, 12, 22, 100, 160, 250, 350, and 500 μm , and 150 and 1400 MHz) of 1056 HSC-FIRST RGs observed with KiDS, HSC, VIKING, ALLWISE, H-ATLAS, FIRST, and TGSS. For optical data, we used MAG_AUTO_U as a u -band photometry that is a default magnitude²⁰ while $g/r/i/z/ycModel_Mag$ were used for g -, r -, i -, z -, and y -band photometry (Bosch et al. 2018; Huang et al. 2018). For NIR data, we used Petrosian (1976) magnitude (see the release note of the VIKING DR3). Each magnitude was corrected for Galactic foreground extinction following Schlegel et al. (1998). The VIKING catalog contains the Vega magnitude of each source, and we converted these to AB magnitude, using offset values Δm ($m_{\text{AB}} = m_{\text{Vega}} + \Delta m$) for J, H , and K_s -band of 0.916, 1.366, and 1.827, respectively.²¹ For MIR and FIR data, `w1-4mpro` were utilized to estimate MIR flux densities (Wright et al. 2010; Toba et al. 2014) while

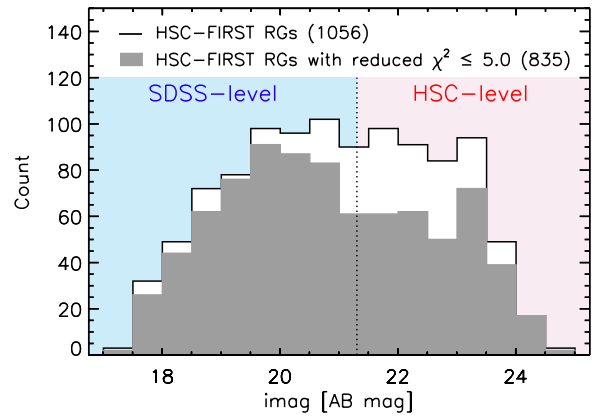


Figure 3. Histogram of i -band magnitude of HSC-FIRST RGs (black line) and those with reduced χ^2 of the SED fitting smaller than 5.0 (gray region), where i -band magnitude is corrected for the Galactic foreground extinction (see Section 2.2). The vertical dashed line is the threshold ($i = 21.3$ mag) between SDSS-level and HSC-level RGs.

F100/160/250/350/500BEST were used for FIR flux densities (see Valiante et al. 2016). ALLWISE catalog contains the Vega magnitude of each source, and we converted these to AB magnitude, using Δm for 3.4, 4.6, 12, and 22 μm of 2.699, 3.339, 5.174, and 6.620, respectively.²² It is known that flux densities at 250, 350, and 500 μm could be boosted especially for faint sources (so-called flux boosting or flux bias) that are caused by a confusion noise and instrument noise. Hence we corrected this effect by using the correction term provided in Table 6 of Valiante et al. (2016). For radio data, FINT and STOTAL were used for flux densities at 1.4 GHz and 150 MHz, respectively (see Helfand et al. 2015; Intema et al. 2017 for more detail). We used flux density at a wavelength when signal-to-noise ratio (S/N) is greater than 3 at that wavelength. If an object was undetected, we put 3σ upper limits at those wavelengths.²³ Although the photometry employed in each catalog is different, their flux densities are expected to trace the total flux densities. Therefore, the influence of different photometry is likely to be small. Nevertheless, it is worth investigating whether or not physical properties can actually be estimated in a reliable way given an uncertainty of each photometry, which will be discussed in Section 4.2.4.

3. Results

3.1. Histogram of i -band Magnitude and Redshift

Figure 3 shows a histogram of i -band magnitude for 1056 HSC-FIRST RGs. Here, we define the “SDSS-level objects” and “HSC-level objects” based on the Galactic foreground extinction-corrected i -band magnitude in the same manner as Yamashita et al. (2018). We call objects with $i < 21.3$ mag the SDSS-level objects as a reference of optically bright RGs, while we call objects with $i \geq 21.3$ mag the HSC-level objects as a reference of optically faint RGs. We found that 577 and 479 objects are classified as the SDSS-level and HSC-level objects, respectively, meaning that we have a statistically

²⁰ <http://www.eso.org/rm/api/v1/public/releaseDescriptions/82>

²¹ <http://casu.ast.cam.ac.uk/surveys-projects/vista/technical/filter-set>

²² http://wise2.ipac.caltech.edu/docs/release/allsky/expsup/sec4_4h.html#conv2ab

²³ CIGALE can handle SED fitting of photometric data with upper limit when one employs the method presented by Sawicki (2012). This method computes χ^2 by introducing the error function (see Equations (15) and (16) in Boquien et al. (2019).

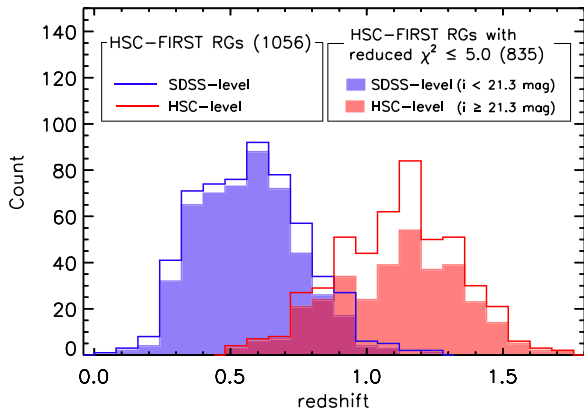


Figure 4. Histogram of redshift of HSC–FIRST RGs (solid line) and those with reduced χ^2 of the SED fitting smaller than 5.0 (shaded region). Red and blue line are the SDSS- and HSC-level objects in 1056 HSC–FIRST RGs. Red and blue regions are those in the 835 subsample (see Section 3.5).

robust sample of optically faint RGs that are newly discovered by the WERGS project (Yamashita et al. 2018).

Figure 4 shows a histogram of redshift for 1056 HSC–FIRST RGs. The mean values of redshift for the SDSS- and HSC-level objects are 0.57 and 1.10, respectively, meaning that HSC-level objects have larger redshift than SDSS-level objects, which is consistent with what Yamashita et al. (2018) reported.

3.2. Result of SED Fitting

Figure 5 shows examples of the SED fitting with CIGALE.²⁴ We confirmed that 568/1056 ($\sim 54\%$) objects have reduced $\chi^2 \leq 3.0$, while 835/1056 ($\sim 79\%$) objects have reduced $\chi^2 \leq 5.0$, which means that the data are moderately well fitted with the combination of the stellar, AGN, SF, and radio components by CIGALE.

We note that each quantity derived by the SED fitting would not be uniquely determined for some objects even if their reduced χ^2 is good enough, because there is a possibility of degeneracy among input parameters. We checked the PDF of each quantity for randomly selected objects. We confirmed that there is basically no prominent secondary peak of their PDFs, suggesting that the derived physical quantities are reliably determined. The physical quantities such as stellar mass and SFR for 1056 HSC–FIRST RGs are also accessible through the online service (see Table 3 for the catalog description).

3.3. Radio and Optical Luminosity as a Function of Redshift

Figure 6(a) shows the rest-frame 1.4 GHz radio luminosity ($L_{1.4 \text{ GHz}}$) of 835 HSC–FIRST RGs as a function of redshift. To make sure of the parameter space of our RGs with respect to previously discovered RGs, RGs selected with the SDSS (Best & Heckman 2012) and RGs found by VLA–COSMOS 3 GHz large project (Smolčić et al. 2017a, 2017b) are also plotted. $L_{1.4 \text{ GHz}}$ in unit of W Hz^{-1} is k -corrected luminosity at rest-frame 1.4 GHz, which is derived by using the following

formula:

$$L_{1.4 \text{ GHz}} = \frac{4\pi d_L^2 F_{1.4 \text{ GHz}}}{(1+z)^{1-\alpha_{\text{radio}}}}, \quad (3)$$

where d_L is luminosity distance, $F_{1.4 \text{ GHz}}$ is observed-frame flux density at 1.4 GHz, and α_{radio} is the radio spectral index we estimated in Equation (1). We note that 190/835 objects have TGSS (150 MHz) data and thus their α_{radio} are securely estimated. If an object did not have α_{radio} due to the non-detection of TGSS, we adopted a typical spectral index of RGs, $\alpha_{\text{radio}} = 0.7$ (e.g., Condon 1992) to estimate $L_{1.4 \text{ GHz}}$. For radio sources selected with either the SDSS or VLA–COSMOS, we also used 0.7 as the spectral index to calculate $L_{1.4 \text{ GHz}}$ if the object did not have radio spectral index (see e.g., Smolčić et al. 2017a). We confirmed that our RG sample distributes much higher redshift ($z > 0.5$) than SDSS-selected RGs, while radio luminosity of our RGs sample is larger than that of VLA–COSMOS radio sources, with a median rms of $2.3 \mu\text{Jy beam}^{-1}$.

Figure 6(b) shows the rest-frame i -band absolute magnitude (M_i) as a function of redshift. M_i of our RG sample was estimated based on the best-fit SED output by CIGALE. Since the VLA–COSMOS catalog (Smolčić et al. 2017a) does not contain M_i , we used the COSMOS2015 catalog (Laigle et al. 2016), in which absolute magnitudes in optical and NIR bands were estimated based on the SED fitting. For SDSS-selected RGs in Best & Heckman (2012), we did not apply for k -correction. But their M_i can be approximately used for absolute magnitude at the rest frame because they are low- z objects. We confirmed that our RG sample has intermediate value of M_i between SDSS-selected and VLA–COSMOS radio sources.

The discrepancy between our RG sample and VLA–COSMOS RG sample in M_i (Figure 6(b)) is much smaller than that in $L_{1.4 \text{ GHz}}$ (Figure 6(a)), suggesting that our RGs tend to trace higher radio-loudness sources, which is one of the advantages of the WERGS project, where even VLA–COSMOS might not be able to trace. In summary, Figure 6 reminds us that our RG survey with HSC and FIRST explores a new parameter space: relatively high- z luminous RGs. We should keep in mind the above parameter space in the following discussions.

3.4. WISE Color–Color Diagram

Figure 7 shows the WISE color–color diagram ([3.4]–[4.6] versus [4.6]–[12]) for 148 HSC–FIRST RGs with $S/N > 3$ in 3.4, 4.6, and $12 \mu\text{m}$ that were drawn from 1056 RG sample. The anticipated MIR colors for various populations of objects are shown with different colors (Wright et al. 2010), which provides us a qualitative view of galaxies. We found that the HSC-level objects tend to be redder than the SDSS-level objects in both colors of [3.4]–[4.6] and [4.6]–[12]. The majority of the SDSS-level objects is located at regions of spirals and LIRGs, while the HSC-level objects are located at regions of Seyferts, starburst galaxies, and ULIRGs.

About 49% of HSC–FIRST RGs with $S/N > 3$ in 3.4, 4.6, and $12 \mu\text{m}$ are located within the AGN wedge defined by Mateos et al. (2012, 2013), who suggested reliable MIR color selection criteria for AGN candidates based on the WISE and wide-angle Bright Ultrahard XMM–Newton survey (BUXS: Mateos et al. 2012). This means that roughly half of the RG sample is outside of the wedge, which is in good agreement

²⁴ Since CIGALE assumed that the maximum wavelength for radio data was rest frame 1 m, CIGALE did not work for our data set, including TGSS (2 m) data for low- z objects. We modified CIGALE code (radio.py) to solve this issue as suggested by Prof. Denis Burgarella through a private communication.

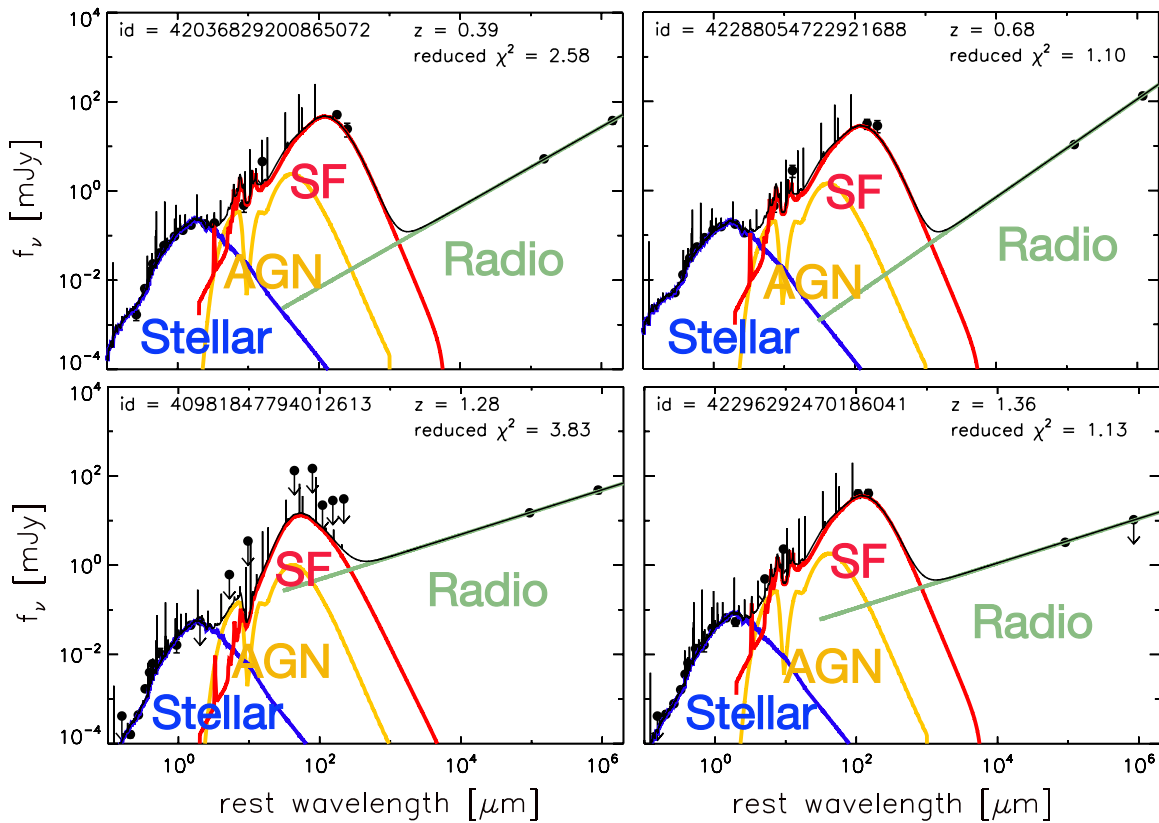


Figure 5. Examples of the SED (flux density as a function of wavelength in rest frame) and result of the SED fitting for our sample. The black points are photometric data where the down arrows mean 3σ upper limit. The blue, yellow, red, and green lines show stellar, AGN, SF, and radio component, respectively. The black solid lines represent the resultant SEDs. We provide best-fit SEDs for all 1056 HSC–FIRST RGs with derived physical properties (see Tables 3 and 4).

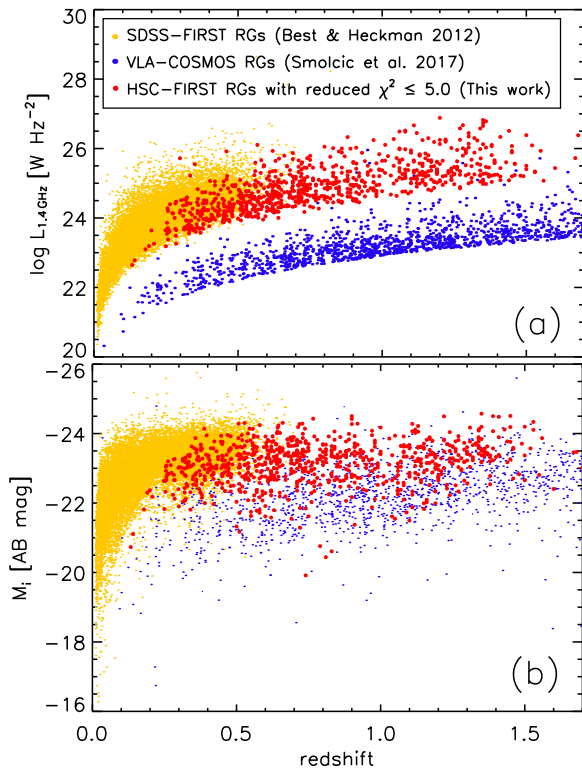


Figure 6. (a) Rest-frame 1.4 GHz radio luminosity and (b) the absolute i -band magnitude at the rest frame as a function of redshift. Yellow and blue circles represent SDSS-detected RGs (Best & Heckman 2012) and RGs discovered by the VLA–COSMOS project (Smolčić et al. 2017a), respectively. Red circles represent HSC–FIRST RGs with reduced $\chi^2 \leq 5.0$.

with previous works on radio-loud galaxies (Gürkan et al. 2014; Banfield et al. 2015), suggesting that the AGN selection based on the AGN wedge seems to be biased toward a subsample among the entire AGN population (see also Toba et al. 2014, 2015; Ichikawa et al. 2017).

What makes the difference between objects inside and outside of the AGN wedge? One possibility is a difference of radio luminosity between them, since radio luminosity is a good tracer of AGN power, as suggested by previous works (e.g., Banfield et al. 2015; Singh et al. 2015; Singh & Chand 2018). We checked this possibility for our sample, where we used the rest-frame radio luminosity at 1.4 GHz that is drawn from Yamashita et al. (2018) assuming a power-law radio spectrum of $f_\nu \propto \nu^{-0.7}$.

Figure 7 shows the histogram of rest-frame 1.4 GHz luminosity, indicating a systematic difference in radio luminosity for objects inside and outside of the AGN wedge. The mean values of rest-frame 1.4 GHz luminosity for objects inside and outside of the AGN wedge are $\log L_{1.4 \text{ GHz}} \sim 24.8$ and $\sim 24.4 \text{ W Hz}^{-1}$, respectively, supporting the previous works. An alternative indicator of AGN power is a radio-loudness that is defined as flux ratio of rest-frame radio and optical band. We used the radio-loudness at rest frame (R_{rest}), a ratio of the rest-frame 1.4 GHz flux to the rest-frame g -band flux as used in Yamashita et al. (2018). Figure 7 also shows the histogram of R_{rest} , indicating a systematic difference in R_{rest} for objects inside and outside of the AGN wedge. The mean values of R_{rest} for objects inside and outside of the AGN wedge are $\log R_{\text{rest}} \sim 2.4$ and ~ 1.9 , respectively, indicating that objects

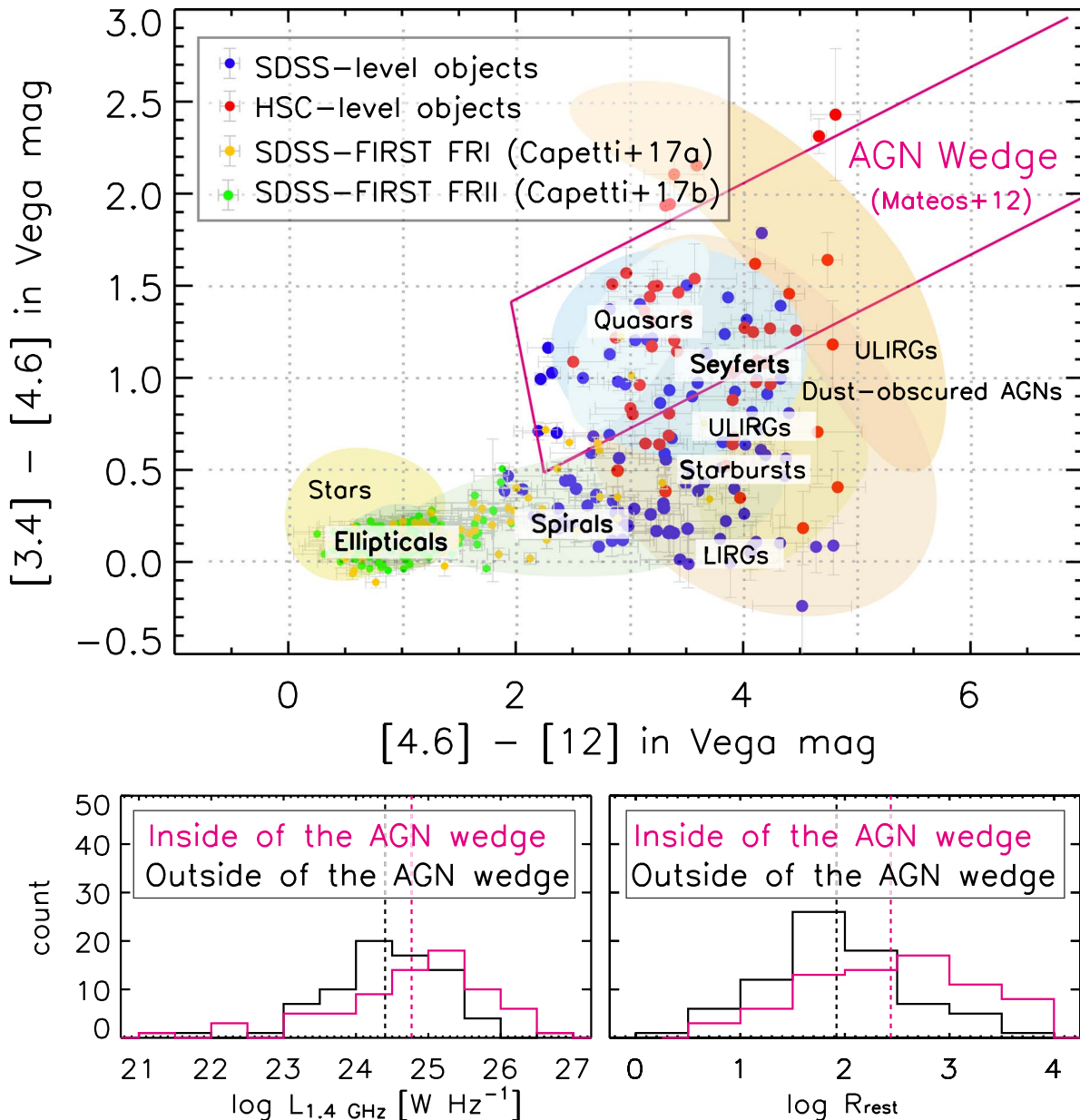


Figure 7. (Top) *WISE* color-color diagram of 148 HSC-FIRST RGs with $S/N > 3$ in 3.4, 4.6, and 12 μm . Blue and red circles are SDSS- and HSC-level RGs, respectively. Yellow and green circles are SDSS-detected FIRST FR I and FR II RGs with $r < 17.8$ mag, respectively, that are obtained from Capetti et al. (2017a, 2017b). Regions with different color shading show typical MIR colors of different populations of objects (Wright et al. 2010). The solid lines illustrate the AGN selection wedge defined from Mateos et al. (2012, 2013). (Bottom) Histogram of rest-frame 1.4 GHz luminosity ($L_{1.4 \text{ GHz}}$) and rest-frame radio-loudness (R_{rest}) for objects inside (magenta) and outside (black) of the AGN wedge. The mean values are shown in dashed lines.

with larger radio-loudness tend to be located in the AGN wedge, as we expected.

We note that there are almost no objects at elliptical galaxies in the *WISE* color-color diagram (Figure 7), which is mainly interpreted as a selection bias of our HSC-FIRST RGs. Since the saturation limit of the HSC for point sources at r -band and i -band are 17.8 and 18.4 mag, respectively (Aihara et al. 2018b), the HSC-FIRST RG sample does not contain those optically bright objects. In Figure 7, we also plot RGs with r -band magnitude smaller than 17.8 mag provided by Capetti et al. (2017a, 2017b), who released Fanaroff & Riley (1974) (FR) I and II RG catalogs²⁵ selected with the SDSS and FIRST. The redshift, optical

absolute magnitude, and radio luminosity range of those RGs are $0.02 < z < 0.15$, $-23.7 < M_R < -20.3$, and $23.3 < \log L_{1.4 \text{ GHz}} [\text{W Hz}^{-1}] < 25.8$, respectively. They show elliptical-like MIR colors, which means that optically too bright objects are located at the region of elliptical galaxies. In addition to the selection bias, there is a possibility that MIR colors of RGs would be different from normal elliptical galaxies. Banfield et al. (2015) reported that $[4.6]-[12]$ color of RGs selected from the Radio Galaxy Zoo²⁶ sample shows significantly redder than that of typical elliptical galaxies. This indicates that the dust emission of RGs may be enhanced compared with normal quiescent elliptical galaxies (see also Goulding et al. 2014; Gürkan et al. 2014). Indeed, Martini et al. (2013) reported that active elliptical

²⁵ Since the catalogs do not contain *WISE* magnitudes, we cross-identified their *WISE* counterparts with a search radius of $3''$ by ourselves.

²⁶ <https://radio.galaxyzoo.org/>

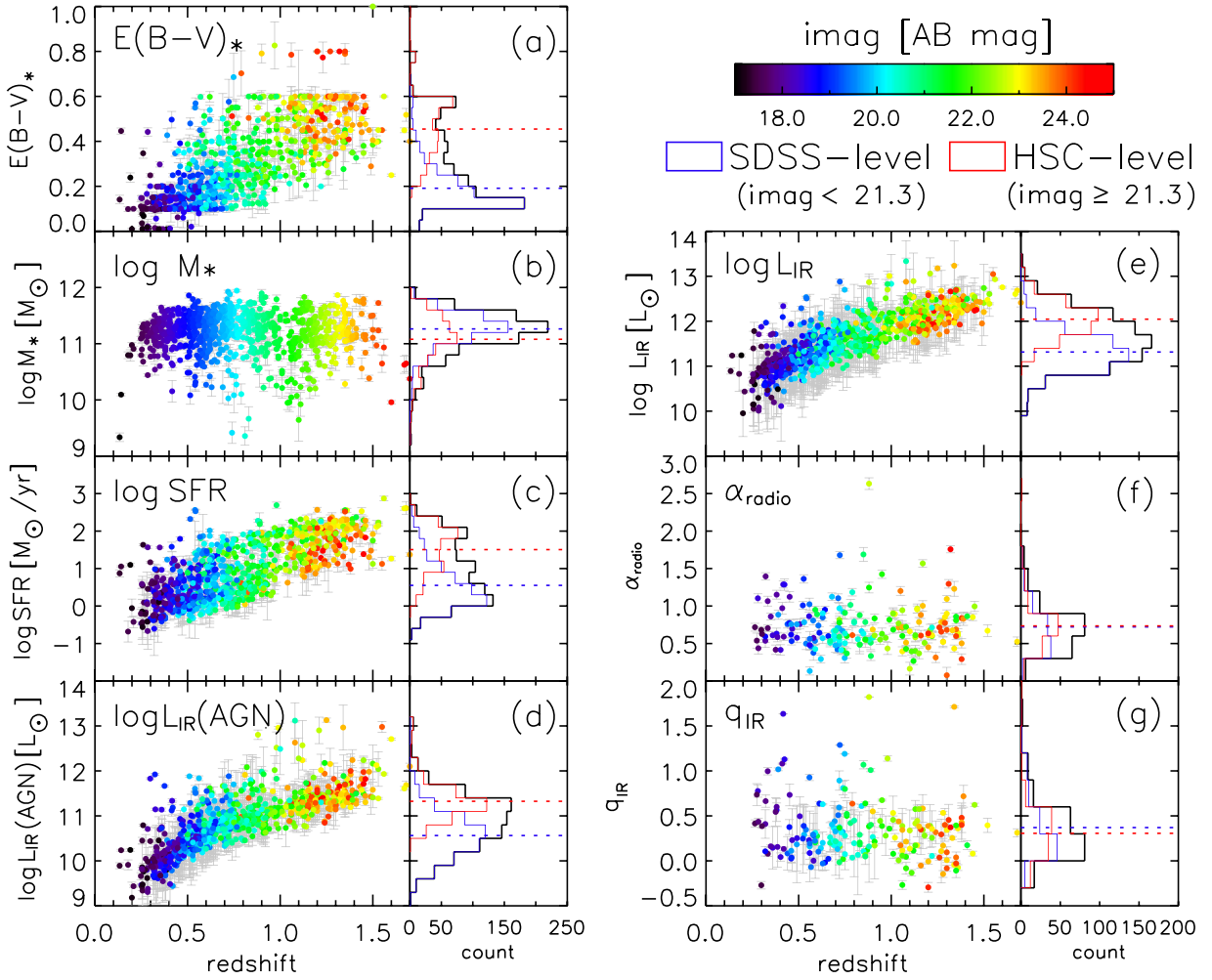


Figure 8. (a) The color excess ($E(B - V)_*$), (b) stellar mass, (c) SFR, (d) IR luminosity contributed from AGNs, (e) total IR luminosity, (f) radio spectral index (α_{radio}), and (g) q_{IR} of HSC–FIRST RGs as a function of redshift. The color code is i -band magnitude. The histograms show the SDSS-level (blue), HSC-level (red), and total (black) objects. The dashed lines are mean values of each quantity for SDSS-level (blue) and HSC-level (red) objects. 835 RGs are plotted in panels (a) to (e) while 190 RGs with FIRST and TGSS data are plotted in panels (f) and (g).

galaxies tend to have a large dust mass compared with inactive elliptical galaxies, which supports the above hypotheses.

3.5. Physical Properties of HSC–FIRST Radio Galaxies

We present the physical properties of HSC–FIRST RGs with being conducted a reliable SED fitting. Hereafter, we will focus on a subsample of 835 HSC–FIRST RGs with reduced χ^2 of the SED fitting smaller than 5.0. In this work, we investigate the following quantities output directly from CIGALE; (i) dust extinction, (ii) stellar mass, (iii) SFR, (iv) AGN luminosity, (v) IR luminosity, and those calculated by ourselves; (vi) radio spectral index, and (vii) $L_{\text{IR}}/L_{\text{radio}}$ coefficient (q_{IR}) as a function of redshift, which are summarized in Figure 8. Among subsample, 501 and 334 objects are classified as the SDSS- and HSC-level objects with a mean redshift of 0.56 and 1.11, respectively (see Figures 3 and 4).

3.5.1. Dust Extinction

Figure 8(a) shows color excess, $E(B - V)_*$ as a function of redshift, where $E(B - V)_*$ is an indicator of dust extinction of host galaxy. We found that there is a clear correlation between redshift and $E(B - V)_*$; optically fainter RGs at high redshift

are affected by larger dust extinction. The mean values of $E(B - V)_*$ of the SDSS- and HSC-level objects are ~ 0.19 and ~ 0.45 , respectively. Indeed, 5 HSC-level objects with mean $E(B - V)_*$ of 0.45 satisfy a criterion of IR-bright dust-obscured galaxies with $S/N > 3$ at $22 \mu\text{m}$ (see e.g., Toba et al. 2015; Toba & Nagao 2016; Toba et al. 2017b, 2018; Noboriguchi et al. 2019).

3.5.2. Stellar Mass

Figure 8(b) shows stellar mass as a function of redshift. The stellar mass of our RG sample does not significantly depend on redshift, and thus the distributions of stellar masses for the SDSS- and HSC-level objects are similar. However, the mean values of stellar mass of the SDSS- and HSC-level objects are $\log(M_*/M_\odot) \sim 11.26$ and ~ 11.08 , respectively, indicating that the HSC-level RGs could tend to have less massive stellar mass compared with the SDSS-level ones.

3.5.3. Star Formation Rate (SFR)

Figure 8(c) shows SFR as a function of redshift. We found that the SFR increases with increasing redshift, and thus the HSC-level objects are systematically larger than those of the

SDSS-level objects. The mean values of SFR of the SDSS- and HSC-level objects are $\log \text{SFR} \sim 0.55$ and $\sim 1.51 M_{\odot} \text{ yr}^{-1}$, respectively. About one-quarter of the HSC-level objects have $\text{SFR} > 100 M_{\odot} \text{ yr}^{-1}$, which is consistent with what was reported in the *WISE* color-color diagram (Figure 7).

3.5.4. AGN Luminosity

Figure 8(d) shows IR luminosity contributed from AGN that is defined as $L_{\text{IR}}(\text{AGN}) = f_{\text{AGN}} \times L_{\text{IR}}$ (Ciesla et al. 2015), where L_{IR} is total IR luminosity (see Section 3.5.5). We found that the $L_{\text{IR}}(\text{AGN})$ increases with increasing redshift, and thus the HSC-level objects seem to have systematically larger AGN luminosity than the SDSS-level objects. The mean values of $\log [L_{\text{IR}}(\text{AGN})/L_{\odot}]$ of the SDSS- and HSC-level objects are ~ 10.56 and ~ 11.32 , respectively.

3.5.5. IR Luminosity

Figure 8(e) shows IR luminosity as a function of redshift. We can see a similar trend to AGN luminosity; IR luminosity increases with increasing redshift, and thus IR luminosities of the HSC-level objects are larger than those of the SDSS-level objects. The mean values of $\log (L_{\text{IR}}/L_{\odot})$ of the SDSS- and HSC-level objects are ~ 11.31 and ~ 12.04 , respectively. This is basically consistent with the fact that the majority of the SDSS and HSC objects are LIRGs and ULIRGs, respectively, reported in Section 3.4.

We note that because our RG sample may be affected by Malmquist bias as shown in Figure 6, the difference particularly in SFR, $L_{\text{IR}}(\text{AGN})$, and L_{IR} between SDSS- and HSC-level objects is basically due to the difference of their redshift distributions. In other words, redshift dependence of L_{IR} , $L_{\text{IR}}(\text{AGN})$, and SFR may be caused by the sensitivity limit of IR bands. On the other hand, it is natural that M_{*} does not show a redshift dependence, because the sensitivity of optical bands with HSC is much deeper than that of the IR bands. If we compare SFR, $L_{\text{IR}}(\text{AGN})$, and L_{IR} of SDSS- and HSC-level objects at an overlapped redshift range ($0.5 < z < 1.0$) (see Figure 4), the differences of mean values of SFR, $L_{\text{IR}}(\text{AGN})$, and L_{IR} are 0.31, 0.30, and 0.25 dex, respectively. We also note that particularly SFR and AGN luminosity would also have an additional uncertainty probably due to a poor constraint of SED given a limited number of data points in MIR and FIR (see Section 4.2.4).

3.5.6. Radio Spectral Index

We present radio spectral index (α_{radio}) and luminosity ratio of IR and radio wavelength (q_{IR}) in the following subsections. Although our sample always has 1.4 GHz data, only one-quarter of objects have 150 MHz data as reported in Section 2.1.6. This means that it is quite hard to determine the radio properties with CIGALE for objects without counterparts of TGSS given a limited number of data points and input parameters. Indeed, the radio spectral index and q_{IR} can be analytically derived by assuming a radio spectrum. So, we focus on 190 HSC-FIRST RGs with both 1.4 GHz and 150 MHz flux densities in Sections 3.5.6 and 3.5.7.

We derive the radio spectral index (α_{radio}) based on Equation (1). Figure 8(f) shows radio spectral index as a function of redshift. There is no clear correlation between α_{radio} and redshift, which is consistent with previous works

(Blundell et al. 1999; Bornancini et al. 2010; Calistro Rivera et al. 2017). The mean value of α_{radio} of 190 HSC-FIRST RGs is ~ 0.73 , which is consistent with what was reported in de Gasperin et al. (2018), who investigated radio spectral index over 80% of the sky based on the NVSS and TGSS. The mean values of α_{radio} of the SDSS- and HSC-level objects are ~ 0.72 and ~ 0.74 , respectively. De Gasperin et al. (2018) reported that the absolute value of radio spectral index increases with radio flux densities. Because radio flux densities at 150 MHz and 1.4 GHz of the HSC-level objects are slightly larger than those of SDSS-level objects, the tiny difference of α_{radio} between SDSS- and HSC-level objects could be explained as a difference of their radio flux densities.

3.5.7. q_{IR}

The ratio of IR and radio luminosity (q_{IR}) is defined as follows (see also Helou et al. 1985; Ivison et al. 2010):

$$q_{\text{IR}} = \log \left(\frac{L_{\text{IR}}/3.75 \times 10^{12}}{L_{1.4 \text{ GHz}}} \right), \quad (4)$$

where L_{IR} is the total IR luminosity in unit of W derived from CIGALE. 3.75×10^{11} is the frequency (Hz) corresponding to $80 \mu\text{m}$, which is used for making q_{IR} a dimensionless quantity. $L_{1.4 \text{ GHz}}$ in unit of W Hz^{-1} is k -corrected luminosity at rest-frame 1.4 GHz, which is derived by Equation (3).

Figure 8(g) shows q_{IR} as a function of redshift. Although there is no clear dependence of q_{IR} on redshift, the mean value of 190 HSC-FIRST RGs is 0.34, which is significantly lower than that of pure SF galaxies whose q_{IR} is $\sim 2-3$ (Yun et al. 2001; Bell 2003; Ivison et al. 2010). This is reasonable because it is known that radio-loud galaxies/AGNs with $\log L_{\text{radio}} > 24 \text{ W Hz}^{-1}$ tend to have significantly small q_{IR} with wide dispersion (Sajina et al. 2008; Calistro Rivera et al. 2017; Williams et al. 2018). We will discuss this point later by using “radio-excess parameter” in Section 4.5.

The mean values of q_{IR} of SDSS- and HSC-level objects are ~ 0.37 and ~ 0.31 , respectively. Calistro Rivera et al. (2017) reported that q_{IR} could be decreased with increasing redshift, while Read et al. (2018) reported that q_{IR} could also be decreased with increasing specific SFR ($\text{sSFR} \equiv \text{SFR}/M_{*}$). Because HSC-level objects are located at higher redshift and they have smaller stellar mass and higher SFR (i.e., higher sSFR), as mentioned in Sections 3.5.2 and 3.5.3, the difference in q_{IR} between SDSS- and HSC-level objects may be explained by the difference of their redshift and sSFR.

3.6. Composite Spectrum

Finally, we show a composite spectrum of the SDSS- and HSC-level objects in Figure 9. Here we performed the median stacking only for 190 HSC-FIRST RGs with reliable radio spectral index. In optical to NIR regime, HSC-level objects are typically less luminous compared with SDSS-level objects, suggesting that HSC-level objects are more affected by dust extinction and their stellar masses are smaller than those of the SDSS-level objects, as reported in Sections 3.5.1 and 3.5.2. Once wavelength is beyond $1 \mu\text{m}$, hot dust emission heated by AGNs and cold dust emission heated by SF will be dominant for HSC-level objects, indicating that HSC-level objects have a large AGN and SF luminosity (i.e., large IR luminosity and SFR)

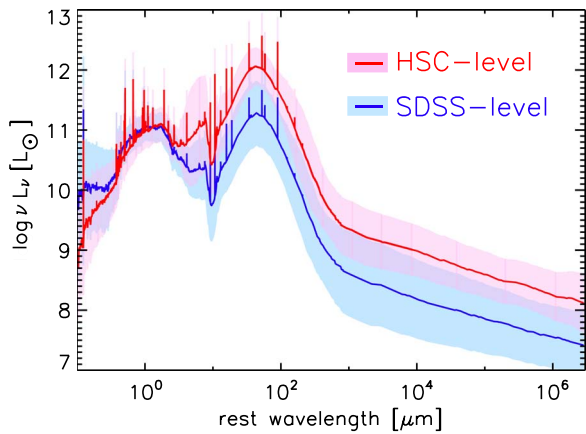


Figure 9. Composite SEDs of SDSS- (blue) and HSC-level (red) RGs with reliable α_{radio} . Shared regions represent standard deviation of the median stacking SEDs. These SED templates are available in Table 4.

compared with SDSS-level objects, as reported in Sections 3.5.3–3.5.5. The best-fit SED template of each HSC–FIRST RG is available in Table 4.

4. Discussion

4.1. Selection Bias

As described in Sections 2 and 3, we selected 1056 objects with reliable redshift and reasonable redshift cut among 1943 RGs and eventually investigated physical properties for 835 RGs with SED fitting. This means that $1943 - 835 = 1108$ ($\sim 57\%$) objects were excluded in this work, which would affect the results we presented above.

To check whether or not we would select a specific population among the entire HSC–FIRST RG sample, we investigated their optical colors. Figure 10 shows a color–color diagram of $r - i$ versus $i - z$ for the entire sample of 1943 objects and subsample of 835 objects. Because the HSC–FIRST RG sample requires all the detections of r , i , and z -band with $S/N > 5$ (see Yamashita et al. 2018), all objects in the entire sample and subsample are plotted in this figure. A two-sided K-S test does not rule out a hypothesis that the distribution of $i - z$ for the subsample of 835 RGs is the same as that for the entire sample of 1943 RGs at $>99.9\%$ significance, which is also supported by a Wilcoxon rank-sum test. On the other hand, those two tests find that two distributions of $r - i$ are statistically different. This could suggest that physical quantities of the subsample of 835 RGs may be (more or less) affected by selection bias, which we should keep in mind in the following discussions.

4.2. Possible Uncertainties

We discuss the possible uncertainties of physical properties derived by CIGALE. We consider the following four things: how (i) the uncertainty of photometric redshift and (ii) the difference in spatial resolution of each catalog affect the derived physical quantities, and comparison of resultant physical quantities with (iii) spectroscopically derived ones and (iv) those derived from the mock catalog. We find that our RG sample is likely to have additional uncertainties, especially for SFR and AGN luminosity. However, it is hard to estimate the exact uncertainty for an individual object because we infer

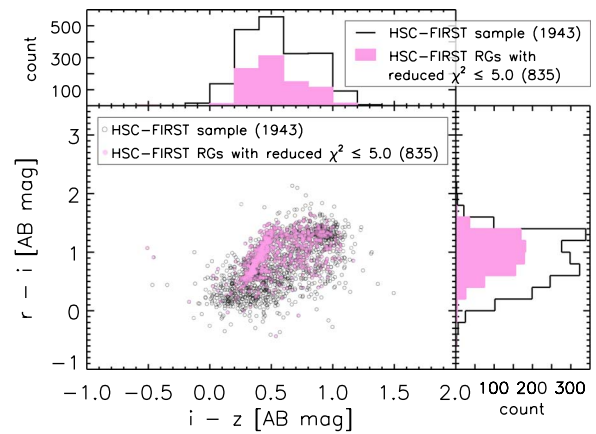


Figure 10. Color–color diagram of $r - i$ and $i - z$. The 1943 HSC–FIRST RG sample, and 835 RGs whose physical properties are studied in this work, are shown in black and magenta circles, respectively. Histogram of each color is also shown with solid lines (an entire sample of 1943 objects) and magenta-shaded regions (a subsample of 835 objects).

the additional uncertainty based on a sort of Monte Carlo simulation. Therefore, we do not include/propagate those possible uncertainties to the original ones output by CIGALE, and focus on a statistical view of possible uncertainties.

4.2.1. Uncertainty of Photometric Redshift

We selected 1056 HSC–FIRST RGs with reliable redshifts as described in Section 2. In particular, we allowed relative errors of photo- z to be at most 10%. Here we discuss how the uncertainty of photo- z affects the derived physical quantities with SED fitting, by performing the following test. First, we assumed a Gaussian distribution with a mean (a photo- z of an object) and sigma (its photo- z error) for each object, and randomly chose one value among the distribution as an adopted redshift. We then conducted the SED fitting with CIGALE under the exact same parameter as what we used in this work for 785 objects whose redshifts came from photo- z with MIZUKI (see Section 2.1.6).

Figure 11 shows the differences in $E(B - V)_*$, $\log M_*$, $\log \text{SFR}$, $\log L_{\text{IR}} (\text{AGN})$, and $\log L_{\text{IR}}$ derived from CIGALE in this work and those derived from CIGALE with random redshift assuming a Gaussian for each object as a function of redshift. The mean values of each quantity are almost zero, while the standard deviations of $\Delta E(B - V)_*$, $\Delta \log M_*$, $\Delta \log \text{SFR}$, $\Delta \log L_{\text{IR}} (\text{AGN})$, and $\Delta \log L_{\text{IR}}$ are 0.03, 0.09, 0.25, 0.10, and 0.10, respectively. We found that $\Delta \log \text{SFR}$ is slightly larger than others due to a relatively large fraction of outliers, suggesting that SFR is most sensitive to uncertainty of photometric redshift. We should keep in mind these possible uncertainties caused by photo- z error.

4.2.2. Influence of Difference in Spatial Resolution of Each Catalog on Physical Quantities

As described in Section 2, we combined multi-wavelength catalogs with different spatial resolutions. In particular, because the angular resolutions of *Herschel* and GMRT are relatively poor, we adopted $10''$ and $20''$ as a search radius to cross-identify with H-ATLAS and TGSS, respectively. If there are multiple IR/radio sources within the search radii but H-ATLAS/TGSS could not resolve them, their FIR and radio (150 MHz) flux densities could be overestimated, which

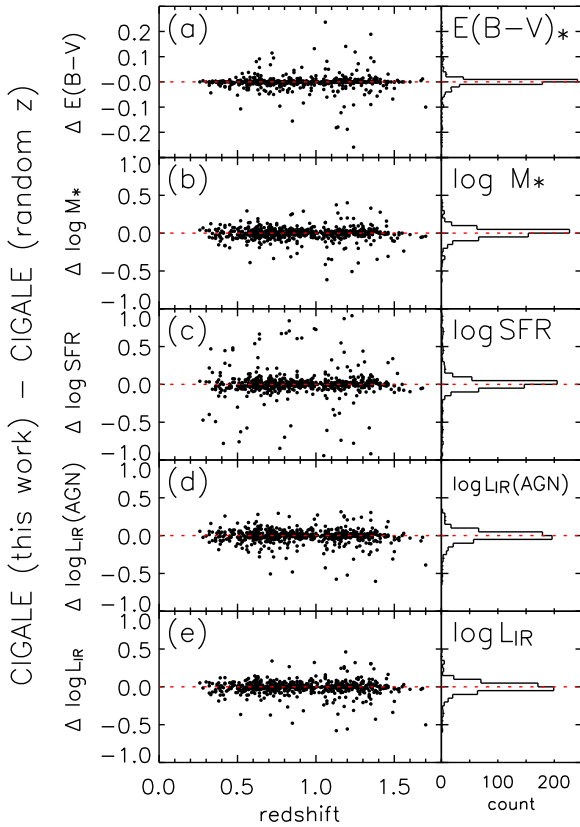


Figure 11. The differences in $E(B - V)_*$, stellar mass, SFR, L_{IR} (AGN), and L_{IR} derived from CIGALE in this work and those derived from CIGALE with a random redshift assigned to each RG assuming a Gaussian probability function for the estimated photometric redshift. (a) $\Delta E(B - V)_*$, (b) $\Delta \log M_*$, (c) $\Delta \log \text{SFR}$, (d) $\Delta \log L_{\text{IR}} (\text{AGN})$, and (e) $\Delta \log L_{\text{IR}}$ as a function of redshift. The right panels show a histogram of each quantity. The red dotted lines are the $\Delta = 0$.

induces a systematic offset for physical quantities, such as IR luminosity and radio spectral index, that are derived by SED fitting (see e.g., Pearson et al. 2018). This effect would be severe for fainter objects at high- z universe (i.e., HSC-level RGs). If we could deblend those sources and re-measure FIR and radio flux densities for an individual object, it would provide us (more or less) an accurate measurement of flux density, although the deblending process may also have an uncertainty, which is beyond the scope of this paper. Therefore, we briefly discuss a possible influence of relatively large beam sizes of H-ATLAS and TGSS on derived physical quantities.

First, we check a possibility of overestimate of FIR flux densities in H-ATLAS by using the ALLWISE catalog, whose sensitivity and angular resolution are better than those of *Herschel* (see Section 2.1.3). We count all nearby *WISE* sources around an object with a search radius of $10''$. If more than one *WISE* source is found around that object, those IR sources would contribute to FIR flux densities that are unresolved by *Herschel*, and their FIR flux densities would be overestimated. We confirm that 89/835 ($\sim 11\%$) objects have multiple *WISE* counterparts within $10''$. Here we test whether or not their IR luminosity has a systematically large value due to boost of their FIR flux densities.

Figure 12 shows the histogram of IR luminosity for 835 HSC–FIRST RGs and 89 objects with multiple *WISE* counterparts. We find that there is no systematic difference between them. The mean IR luminosity of 89 objects is $\log(L_{\text{IR}}/L_{\odot}) \sim 11.48$,

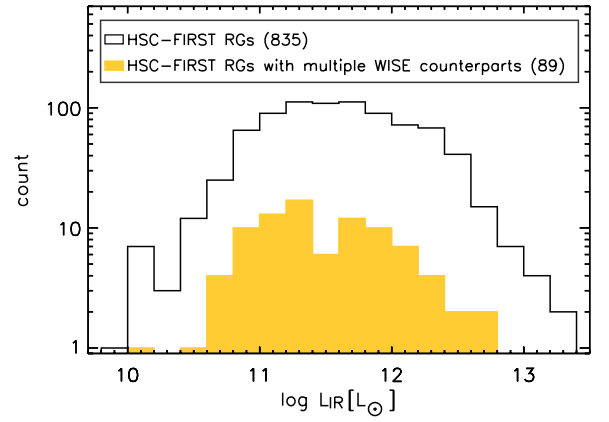


Figure 12. The distribution of IR luminosity for HSC–FIRST RGs. The yellow-shaded region corresponds to objects with multiple *WISE* counterparts.

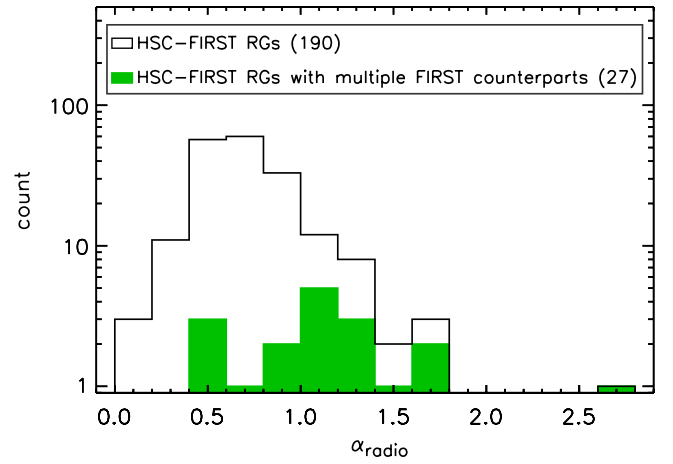


Figure 13. The distribution of radio spectral index for HSC–FIRST RGs. The green-shaded region corresponds to objects with multiple FIRST counterparts.

which is in good agreement with that of all HSC–FIRST RGs, suggesting that poor angular resolution of H-ATLAS does not significantly affect the measurement of FIR flux densities.

Next, we check a possibility of overestimate of radio flux density at 150 MHz in TGSS by using the FIRST catalog, whose sensitivity and angular resolution ($6''$) are better than those of GMRT. We count all nearby FIRST sources around an object with a search radius of $20''$, and confirm that 27/190 ($\sim 14\%$) objects have multiple FIRST counterparts within $20''$. Here we test whether or not their radio spectral index (α_{radio}) have systematically large value due to a boost of their 150 MHz flux densities. Figure 13 shows the histogram of radio spectral index for 190 HSC–FIRST RGs, and 27 objects with multiple FIRST counterparts. We find that 27 objects systematically have large α_{radio} . Their mean α_{radio} is 1.19, which is significantly larger than that of all HSC–FIRST RGs, suggesting that radio spectral indices of some RGs have a potential to be overestimated. We note that radio morphology of some RGs looks different from optical/IR; for example, they have radio lobes in addition to radio core, which makes the cross-identification between optical and radio complicated. We visually checked radio images to see how many RGs could have that kind of complex morphology. We found that 48/835 ($\sim 5.7\%$) of our RGs sample would have such morphology. Their mean α_{radio} is 1.05, which is also larger than the typical value of HSC–FIRST RGs, suggesting that flux

density at 150 MHz taken by TGSS with poor spatial resolution may measure even emission from lobes, and thus that their α_{radio} may be overestimated.

4.2.3. Comparison with Spectroscopically Derived Quantities

We derived $E(B - V)_*$, stellar mass, and SFR based on photometric data with SED fitting, as presented in Sections 2 and 3. Here, we check the consistency between those quantities derived based on CIGALE and spectroscopic data. We compiled the stellar masses from the SDSS DR12 `stellarMassPCAWiscBC03` table, which are derived using the method of Chen et al. (2012) with the SSP models of Bruzual & Charlot (2003). Because a default IMF adopted in the `stellarMassPCAWiscBC03` table is Kroupa (2001), we converted their Kroupa stellar masses to those with Chabrier (2003) IMF by subtracting 0.05 dex from the logarithm of stellar masses, in the same manner as Chen et al. (2012). For $E(B - V)_*$, we utilized the SDSS DR12 `emissionLinesPort` table, in which objects are fitted using an adaptation of the publicly available Gas AND Absorption Line Fitting (GANDALF; Sarzi et al. 2006) and penalized PiXel Fitting (pPXF; Cappellari & Emsellem 2004). Stellar population models for the continuum come from Maraston & Strömbäck (2011) and Thomas et al. (2011). For SFR, we used an emission line-based SFR where we selected [O II] $\lambda\lambda 3726, 3729$ doublet, which is known as a good indicator of SFR (e.g., Kennicutt 1998). We used a relation suggested by Kewley et al. (2004) to estimate [O II]-based SFR ($\text{SFR}_{[\text{O II}]}$):

$$\text{SFR}_{[\text{O II}]} = (6.58 \pm 1.65) \times 10^{-42} L_{[\text{O II}]}^{\text{cor}}, \quad (5)$$

where $L_{[\text{O II}]}^{\text{cor}}$ is the extinction-corrected [O II] luminosity in units of erg s^{-1} , which is calculated using the following formula (see Calzetti et al. 1994; Domínguez et al. 2013):

$$L_{[\text{O II}]}^{\text{cor}} = L_{[\text{O II}]}^{\text{obs}} 10^{0.4k_{[\text{O II}]} E(B-V)_{\text{gas}}}, \quad (6)$$

where $L_{[\text{O II}]}^{\text{obs}}$ is the observed [O II] luminosity, $k_{[\text{O II}]}$ is the extinction value at $\lambda = 3727 \text{ \AA}$ provided by Calzetti et al. (2000), and $E(B - V)_{\text{gas}}$ is the color excess estimated from emission lines. The observed [O II] flux and $E(B - V)_{\text{gas}}$ are tabulated in `emissionLinesPort` table.

Figure 14 shows the differences in $E(B - V)_*$, stellar mass, and SFR derived from CIGALE and those derived from the SDSS spectroscopic data (i.e., the `stellarMassPCAWiscBC03` and `emissionLinesPort` tables). We found that $E(B - V)_*$ derived from CIGALE is slightly overestimated by 0.03 dex, while $\log M_*$ derived from CIGALE is significantly underestimated by 0.27 dex (see Figures 14(a) and (b)). However, this offset is consistent with what was reported in Chen et al. (2012), who compared stellar masses derived from their method with principal component analysis (PCA) and those derived from the SDSS 5-band photometry. They reported that the PCA-based stellar mass shows a systematically positive offset. We also note that assumed SFH in Chen et al. (2012) differs from that in this work, which would also induce a systematic difference of $E(B - V)_*$ and stellar mass. The mean value of $\Delta \log \text{SFR}$ is 0.06, which is negligibly small, while its standard deviation is 0.77, which is very large, as shown in Figure 14(c). Because a typical uncertainty of [O II]-based SFR is about 0.6 dex, whether or not the above large offset is significant is still unclear. Another possibility of the large dispersion of $\Delta \log \text{SFR}$ may be a contamination of

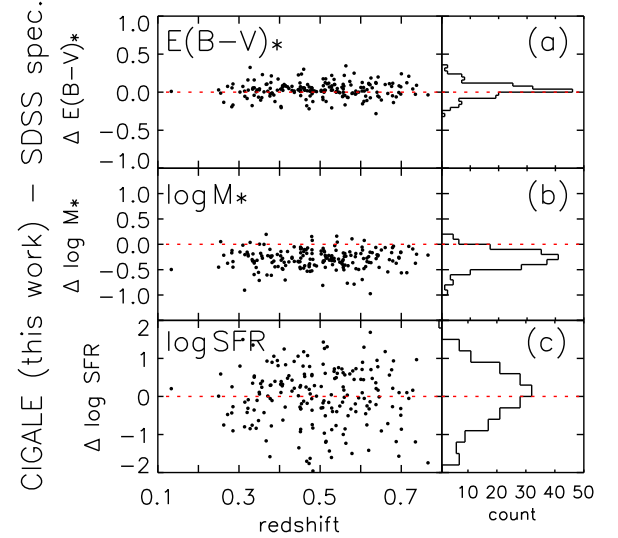


Figure 14. The differences in $E(B - V)_*$, stellar mass, and SFR derived from CIGALE and those derived from the SDSS DR12 spectroscopic data (`stellarMassPCAWiscBC03` and `emissionLinesPort` table). (a) $\Delta E(B - V)_*$, (b) $\Delta \log M_*$, and (c) $\Delta \log \text{SFR}$ as a function of redshift. The right panels show a histogram of each quantity. The red dotted lines are the $\Delta = 0$.

the AGN extended emission line region. Recently, Maddox (2018) reported that [O II] is not always a good indicator of SFR for AGNs when strong [Ne V] $\lambda 3426$ is present in the AGN spectrum. Roughly a quarter of the RG sample with SDSS spectra has a prominent [Ne V] line with $S/N > 5.0$, and thus their [O II]-based SFR would have a large uncertainty. Nevertheless, we should keep in mind the possibility of those systematic uncertainties. On the other hand, this test is only appreciable to SDSS-level objects ($z < 0.8$) and thus we need to check whether or not the resultant quantities of HSC-level objects is reliable through another way (see Section 4.2.4).

4.2.4. Comparison with Physical Quantities Derived from Mock Catalog

Since CIGALE has a procedure to assess whether or not physical properties can actually be estimated in a reliable way through the analysis of a mock catalog, we here discuss the influence of photometric uncertainty on the derived physical quantities. To make the mock catalog, CIGALE first uses the photometric data for each object based on the best-fit SED, and then modifies each photometry by adding a value taken from a Gaussian distribution with the same standard deviation as the observation. This mock catalog is then analyzed in the exact same way as the original observations (see Boquien et al. 2019 for more detail).

Figure 15 shows the differences in $E(B - V)_*$, stellar mass, SFR, L_{IR} (AGN), and L_{IR} derived from CIGALE in this work and those derived from the mock catalog as a function of redshift. The mean values of $\Delta E(B - V)_*$, $\Delta \log M_*$, $\Delta \log \text{SFR}$, $\Delta \log L_{\text{IR}}$ (AGN), and $\Delta \log L_{\text{IR}}$ are 0.03, -0.03 , 0.14, 0.15, and 0.32, respectively. In particular, we can see a secondary peak in $\Delta \log \text{SFR}$ and $\Delta \log L_{\text{IR}}$ (AGN) regardless of redshift. This suggests that SFR and AGN luminosity are sensitive to uncertainty of photometry, which may be a limitation of our SED fitting method given a limited number of data points in MIR and FIR.

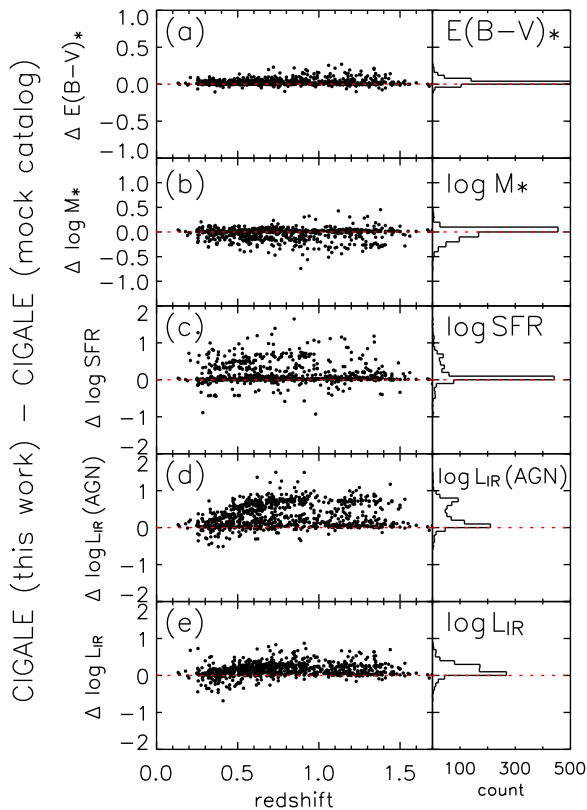


Figure 15. The differences in $E(B - V)_*$, stellar mass, SFR, L_{IR} (AGN), and L_{IR} derived from CIGALE in this work and those derived from the mock catalog. (a) $\Delta E(B - V)_*$, (b) $\Delta \log M_*$, (c) $\Delta \log \text{SFR}$, (d) $\Delta \log L_{\text{IR}}$ (AGN), and (e) $\Delta \log L_{\text{IR}}$ as a function of redshift. The right panels show a histogram of each quantity. The red dotted lines are the $\Delta = 0$.

4.3. Stellar Mass and SFR Relation as a Function of Redshift

It is well known that the stellar mass and SFR of galaxies are correlated, and the majority of galaxies follow a relation called the main sequence (MS) (e.g., Brinchmann et al. 2004; Daddi et al. 2007; Elbaz et al. 2007). This relation has evolved toward high redshift (e.g., Speagle et al. 2014; Lee et al. 2015; Tomczak et al. 2016). Galaxies undergoing active SF (so-called starburst galaxies) lie above the MS, while those without active SF (so-called passive galaxies) lie below the MS. The stellar mass and SFR are fundamental physical quantities of galaxies, and thus investigating the relation (M_* –SFR) provides us a clue of galaxy evolution. Here we investigate the stellar mass and SFR relation for HSC–FIRST RGs to see if there is any difference between SDSS- and HSC-level RGs. Because stellar masses and SFRs of RGs depend on i -band magnitude and redshift (see Figures 8(b) and (c)), we check M_* –SFR for SDSS- and HSC-level RGs as a function of redshift.

Figure 16 shows the stellar mass and SFR for HSC–FIRST RGs as a function of redshift. The M_* –SFR relations of MS galaxies as a function of redshift are also plotted, and are provided by Pearson et al. (2018). They measured stellar mass and SFR by using multi-wavelength data including UV to FIR. They also employed CIGALE to derive those quantities by assuming the same SFH, SSP, and IMF as this work. This is important to do a fair comparison because different assumptions of SFH, SSP, and IMF induces a systematic offset for stellar mass and (particularly) SFR (e.g., Maraston et al. 2010).

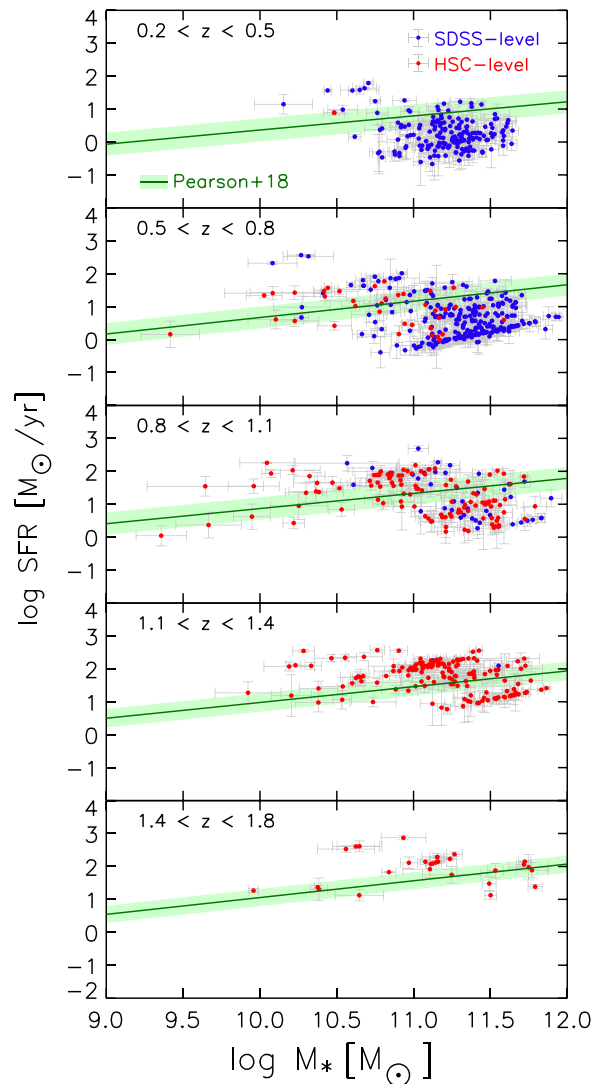


Figure 16. Stellar mass and SFR for HSC–FIRST RGs as a function of redshift. Blue and red points are the SDSS- and HSC-level RGs, respectively. The green lines are the main sequences (MSs) of SF galaxies at each redshift range provided by Pearson et al. (2018). The green-shaded regions correspond to an intrinsic scatter of each green line.

At low redshift ($0.2 < z < 0.8$), the majority of the SDSS-level objects lie below the MSs, indicating that they are passive galaxies, which is consistent with a classical view of RGs in the local universe (Best & Heckman 2012). At intermediate redshift ($0.8 < z < 1.1$)—that is, an overlapped redshift regime between SDSS- and HSC-level RGs—they are widely distributed on the M_* –SFR plane: from passive, MS, to starburst galaxies. We find that there is no clear difference between SDSS- and HSC-level RGs. At high redshift ($1.1 < z < 1.7$), the majority of the HSC-level RGs are located at MS, although some HSC-level RGs lie above the MS of SF galaxies. Eventually, we confirmed that our HSC–FIRST RG sample contains various populations, including classical passive RGs, normal SF galaxies, and starburst galaxies.

4.4. AGN Luminosity and SFR Relation as a Function of Redshift

We investigate the relation between AGN and SF activity for HSC–FIRST RGs. Many studies have demonstrated that AGN activity (e.g., AGN bolometric luminosity) correlates with SF

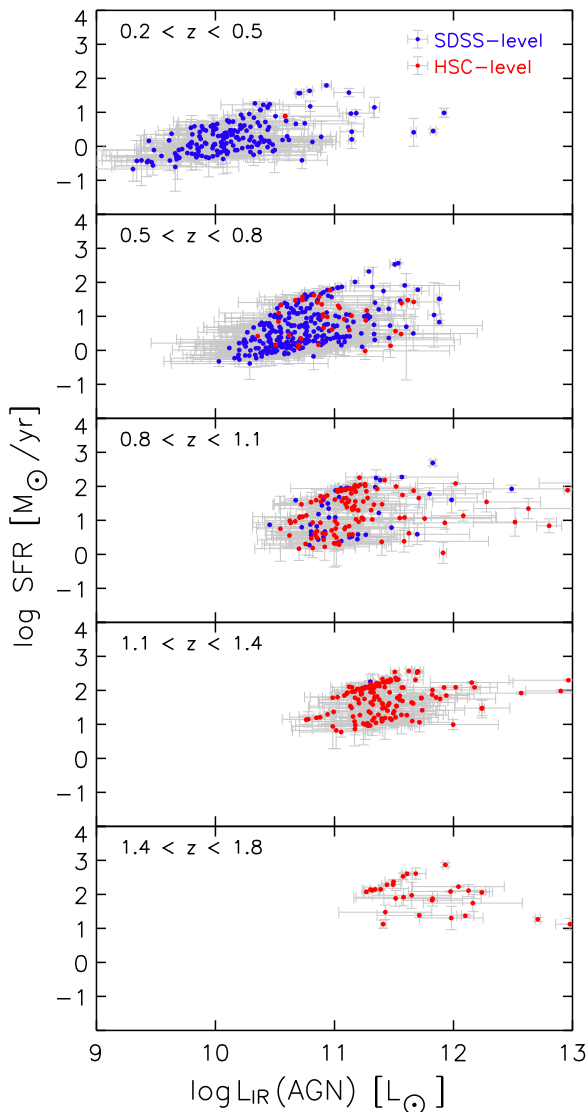


Figure 17. The relationship between IR luminosity contributed from AGN and SFR for HSC-FIRST RGs as a function of redshift. Blue and red points are the SDSS- and HSC-level RGs, respectively.

activity (e.g., FIR luminosity), especially for luminous AGNs (e.g., Netzer 2009; Shao et al. 2010; Rosario et al. 2012; Stanley et al. 2017; Ueda et al. 2018). Although we already showed AGN luminosity and SFR for SDSS- and HSC-level RGs (see Figure 8), we here investigate their relationship as a function of redshift in order to check that there is a difference in SDSS- and HSC-level RGs.

Figure 17 shows the relation between IR luminosity contributed from AGN, $L_{\text{IR}}(\text{AGN})$, and SFR as a function of redshift, where $L_{\text{IR}}(\text{AGN})$ and SFR are derived in Sections 3.5.4 and 3.5.3, respectively. We find that there is no clear difference in SDSS- and HSC-level RGs at a given redshift.

4.5. Radio-excess Parameter

In Section 3.5.7, we found that q_{IR} of HSC-FIRST RGs is significantly lower than that of pure SF galaxies. Del Moro et al. (2013) defined “radio-excess sources” with $q_{\text{IR}} < 1.68$, which corresponds to 3σ deviation from the peak of the distribution for their sample. According to their criterion, all of our HSC-FIRST RGs with TGSS data are radio-excess

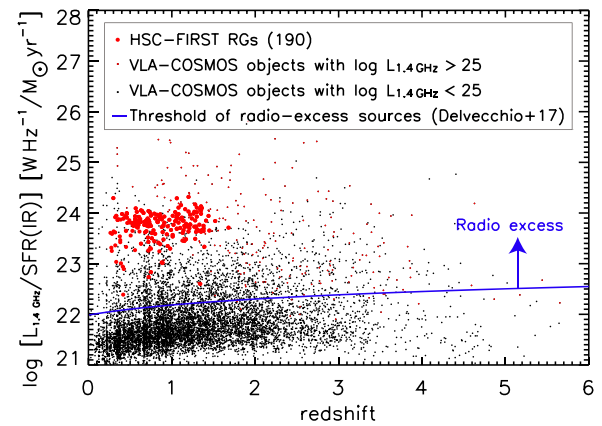


Figure 18. $q_{\text{excess}} = \log [L_{1.4 \text{ GHz}}/\text{SFR}(\text{IR})]$ (radio-excess parameter) as a function of redshift. Small dots are radio sources discovered by the VLA-COSMOS 3 GHz large project (Smolčić et al. 2017a). Large circles with red color are our HSC-FIRST RGs. Small red dots mean VLA-COSMOS sources with $\log L_{1.4 \text{ GHz}} > 25 \text{ W Hz}^{-1}$. The blue line is the threshold of radio-excess sources that is formulated as $q_{\text{excess}} = 21.984 \times (1+z)^{0.013}$ (Delvecchio et al. 2017). Objects with q_{excess} greater than this threshold are classified as radio-excess sources.

sources. Even if we calculate q_{IR} for objects without TGSS data by adopting mean value of radio spectral index, about 98% of objects remain radio-excess sources. Why are almost all HSC-FIRST RGs radio-excess sources? We report that this is due to our selection bias by comparing with much fainter RGs.

Here, we define “radio-excess parameter,” which was introduced in Delvecchio et al. (2017):

$$q_{\text{excess}} = \log \left(\frac{L_{1.4 \text{ GHz}}}{\text{SFR}(\text{IR})} \right), \quad (7)$$

where $L_{1.4 \text{ GHz}}$ is what we obtained in Equation (3). SFR (IR) is derived from IR luminosity contributed from SF in the same manner as Toba et al. (2017c) (see also Kennicutt 1998; Salim et al. 2016):

$$\log \text{SFR}(\text{IR}) = \log L_{\text{IR}}(\text{SF}) - 9.966. \quad (8)$$

Delvecchio et al. (2017) defined a threshold of radio-excess sources as a function of redshift; if an object at a redshift z has $q_{\text{excess}} > 21.984 \times (1+z)^{0.013}$, the object is classified as a radio-excess source. This definition is fairly consistent with that of Delvecchio et al. (2017); radio-excess objects based on their selection satisfy the criterion of Delvecchio et al. (2017), i.e., their q_{IR} values are less than 1.68.

Figure 18 shows radio-excess parameter as a function of redshift for HSC-FIRST objects with TGSS data. Low-luminosity radio sources found by the VLA-COSMOS 3 GHz large project (Smolčić et al. 2017a, 2017b) are also plotted. We found that almost all RGs with $\log L_{1.4 \text{ GHz}} > 25.0 \text{ W Hz}^{-1}$ are classified as radio-excess sources. Because 156/190 ($\sim 82\%$) of the HSC-FIRST RG sample has $\log L_{1.4 \text{ GHz}} > 25.0 \text{ W Hz}^{-1}$, we conclude that the fact that our sources are radio-excess objects may be due to the flux cut ($f_{1.4 \text{ GHz}} > 1.0 \text{ mJy}$) for HSC-FIRST RGs (see Section 2.1). We also confirm that the origin of radio excess is due to AGNs that boost radio luminosity, because their SFRs are basically normal SF galaxies (see Section 3.5.3). Indeed, Del Moro et al. (2013) reported that the fraction of radio-excess objects increases with X-ray luminosity. They also found that roughly half of these radio-excess AGNs are not detected in the deep *Chandra* X-ray

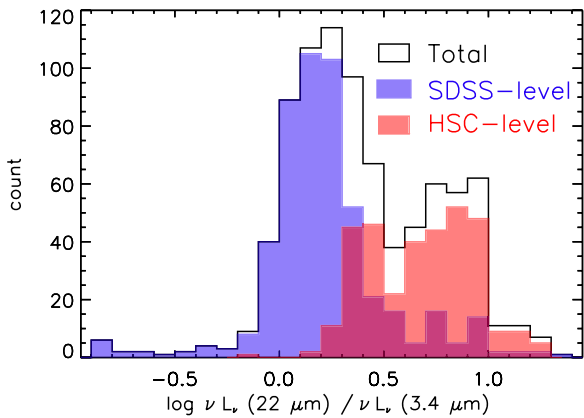


Figure 19. Ratio of rest-frame 22 and 3.4 μm luminosities for SDSS-level (red), HSC-level (blue), and total (black) RGs.

data. Taking the fact that HSC-level objects have large $E(B - V)_*$ (see Section 3.5.1) into account, these results could indicate that particularly some HSC-level RGs harbor heavily obscured AGNs.

4.6. Accretion Rate

We discuss the BH mass accretion rate of SDSS- and HSC-level objects. RGs are classified into low-excitation RGs (LERGs) and high-excitation RGs (HERGs) based on their optical spectra (e.g., Laing 1994; Buttiglione et al. 2010). Many works have studied physical properties of LERGs and HERGs, and have revealed that HERGs tend to have low stellar mass and high SFR, while LERGs tend to reside in denser environments (e.g., Best & Heckman 2012; Janssen et al. 2012; Ching et al. 2017). In terms of *WISE* colors, LERGs are basically distributed at ellipticals/spirals/LIRGs, while HERGs are basically distributed at Seyferts/starbursts/ULIRGs (Gürkan et al. 2014; Yang et al. 2015; Mingo et al. 2016; Whittam et al. 2018). This result could indicate that the relation between LERGs and HERGs is likely to be similar to that of SDSS- and HSC-level objects (e.g., Prescott et al. 2018). Because the observational characteristics of HERGs and LERGs are mainly driven by the accretion rate on to the SMBH (Best & Heckman 2012), it is expected that the accretion rate of HSC-level objects would differ from that of SDSS-level objects.

First, we checked a difference of observational quantities, the ratio of rest frame 22 and 3.4 μm in the same manner as Gürkan et al. (2014). Because the rest-frame 22 μm luminosity is a good tracer of AGN luminosity, while rest-frame 3.4 μm luminosity roughly corresponds to stellar mass, their luminosity ratio is a proxy of the Eddington-scaled accretion rate. Rest-frame 3.4 and 22 μm luminosities were derived from CIGALE, which conducted a convolution integral of best-fit SED with filter response functions of *WISE* W1 and W4 bands.

Figure 19 shows a histogram of luminosity ratio of rest frame 22 and 3.4 μm for HSC-FIRST RGs. There is a clear difference between SDSS- and HSC-level objects; the luminosity ratio of HSC-level objects is systematically larger than that of SDSS-level objects. This result suggests that HSC-level objects have a high Eddington-scaled accretion rate compared with SDSS-level objects.

Next, we performed a rough estimate of Eddington ratio (λ_{Edd}) of our RG sample, in the same manner as Toba et al. (2017a)

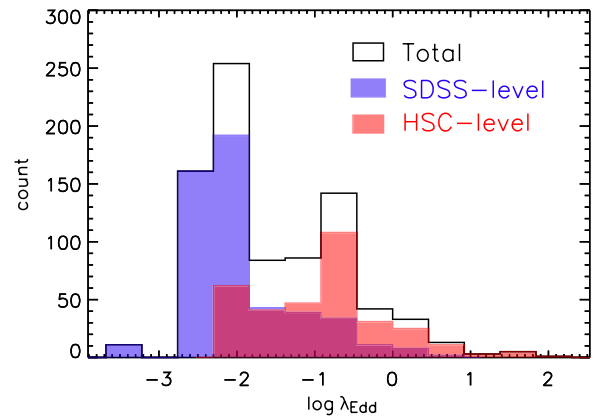


Figure 20. A histogram of Eddington ratio for SDSS-level (red), HSC-level (blue), and total (black) RGs.

(see also Mingo et al. 2016; Whittam et al. 2018). The BH mass (M_{BH}) was estimated from stellar mass by using an empirical relation with a scatter of 0.24 dex, reported in Reines & Volonteri (2015):

$$\log(M_{\text{BH}}/M_{\odot}) = 7.45 + 1.05 \times \log(M_*/10^{11} M_{\odot}), \quad (9)$$

and we converted it to Eddington luminosity (L_{Edd}). The bolometric luminosity (L_{bol}) is estimated by integrating the best-fit SED template of AGN component output by CIGALE over wavelengths longward of Ly α .

Figure 20 shows a histogram of λ_{Edd} ($=L_{\text{bol}}/L_{\text{Edd}}$) of HSC-FIRST RGs. The HSC-level objects clearly have a large Eddington ratio compared with SDSS-level objects. The mean values of (λ_{Edd}) SDSS- and HSC-level objects are -1.95 and -0.94 , respectively, indicating that HSC-level objects have actively growing SMBHs in their center. We note that a fraction of HSC-level objects have $\lambda_{\text{Edd}} > 1$. Their Eddington ratios may be overestimated due to underestimation of their black hole mass. We used the empirical relation of stellar mass and BH mass provided by Reines & Volonteri (2015), which is optimized for broad-line AGNs with $6 < \log(M_{\text{BH}}/M_{\odot}) < 8$ at $z < 0.1$. If we use another empirical relation for elliptical galaxies provided by Reines & Volonteri (2015), the resultant BH masses are roughly one order of magnitude larger than those we reported above. McLure et al. (2006) also reported that the BH to bulge mass ratio of radio-loud AGNs increases with increasing redshift; given a bulge mass of an object at $z > 1$, its BH mass is larger than that of the local universe. Because a large fraction of HSC-level objects are radio-loud AGNs at $z > 1$, their BH masses would be underestimated. Nevertheless, the difference in Eddington ratio between SDSS- and HSC-level objects seems to be significant even if the BH mass of HSC-level objects would be underestimated by 0.5–1 dex.

4.7. Duty Cycle of the HSC-FIRST RGs

Finally, we briefly discuss the duty cycle of SDSS- and HSC-level RGs and their evolutionary link. It should be noted that because our RG sample might be affected by systematic uncertainty and selection bias, as discussed in Sections 4.1 and 4.2, the estimated duty cycle may also have a large uncertainty. Nevertheless, it is worth discussing how the RG sample discovered by the HSC and FIRST can be interpreted in the framework of galaxy formation and evolution. We selected

501 SDSS-level RGs at $0.1 < z < 1.2$, while 334 HSC-level RGs were at $0.5 < z < 1.7$ in $\sim 94.7 \text{ deg}^2$. The corresponding co-moving volume density of SDSS- and HSC-level RGs is 8.9×10^{-7} and $3.3 \times 10^{-7} \text{ cMpc}^{-3}$, respectively.²⁷ On the other hand, the range of stellar mass derived by CIGALE for SDSS-level RGs is $11.0 < \log(M_*/M_\odot) < 11.6$, while that for HSC-level RGs is $10.6 < \log(M_*/M_\odot) < 11.5$. According to the stellar mass function of massive galaxies provided by Kajisawa et al. (2009),²⁸ the volume density of galaxies with same redshift and stellar mass range as SDSS- and HSC-level RGs is 3.1×10^{-4} and $7.9 \times 10^{-4} \text{ cMpc}^{-3}$, respectively. If we assume that massive galaxies with $\log(M_*/M_\odot) \sim 11.0$ have an experience of HSC–FIRST RG phase at least once during a redshift range in which they are observed (i.e., 6.95 and 4.82 Gyr for SDSS- and HSC-level RGs, respectively), the resultant duty cycle of SDSS- and HSC-level RGs is 0.003 ($\sim 19.6 \text{ Myr}$) and 0.0004 ($\sim 2.0 \text{ Myr}$), respectively.

Because the stellar mass of the vast majority of the optically faint RGs is indeed as massive as the bright RGs, there may be a possibility that they are evolutionally linked. We may be witnessing short duty-cycle phenomena, which may be able to quench SF activity at $z \sim 1.0$ or keep quenching SF activity at $z \sim 0.5$ and to activate AGNs in relatively massive galaxies. On the other hand, the duty cycle of HSC-level RGs seems to be too short as a duration of radio jet activity in powerful RGs. One possibility is that our assumption to derive the duty cycle (i.e., massive galaxies have an experience of HSC–FIRST RG phase at least once during their redshift range) is too strict. If we assume that massive galaxies would have an experience of HSC–FIRST RG phase at least once in the history of the universe, the duty cycle could be about 10 Myr.

5. Summary

In this work, we investigated the physical properties of optically faint RGs with $f_{1.4 \text{ GHz}} > 1 \text{ mJy}$ selected by HSC and FIRST, whose nature has been poorly understood so far. We constructed a subsample of 1056 RGs with reliable redshift and multi-wavelength data from optical to radio, among a sample of 1943 RGs in $\sim 100 \text{ deg}^2$. By conducting the SED fitting with CIGALE, we obtained reliable physical quantities of 835 objects at $0 < z \leq 1.7$. Thanks to the deep optical imaging with HSC, we are able to investigate physical quantities of luminous RGs even at $z > 0.5$, which cannot be probed by previous optical surveys. We investigate the physical quantities as a function of redshift. In addition, we discuss the physical difference between optically bright, SDSS-level RGs with $i < 21.3 \text{ mag}$ (mean $z = 0.57$) and optically faint, HSC-level RGs with $i \geq 21.3 \text{ mag}$ (mean $z = 1.10$). We summarize resultant properties (mean value of each quantity for SDSS- and HSC-level RGs and total RG sample) in Table 2. The main results are as follows.

1. Color excess, $E(B - V)_*$, increases with increasing redshift, and thus $E(B - V)_*$ of HSC-level objects is larger than that of SDSS-level objects (Section 3.5.1).
2. Stellar mass is not significantly correlated with redshift. But the mean stellar mass of HSC-level objects is slightly smaller than that of SDSS-level objects. On the other hand, SFR increases with increasing redshift, and thus

²⁷ cMpc is a co-moving distance in unit of Mpc.

²⁸ Kajisawa et al. (2009) assumes Salpeter (1955) IMF. So, we re-calculated the volume density based on Chabrier IMF.

Table 2
Summary of Physical Properties (the Mean Value of Each Quantity) of 835 HSC–FIRST RGs

Physical Properties	SDSS-level	HSC-level	Total
$E(B - V)_*$	0.19	0.45	0.30
$\log(M_*/M_\odot)$	11.26	11.08	11.19
$\log \text{ SFR } [M_\odot \text{ yr}^{-1}]$	0.55	1.51	0.93
$\log [L_{\text{IR}}(\text{AGN})/L_\odot]$	10.56	11.32	10.87
$\log(L_{\text{IR}}/L_\odot)$	11.31	12.04	11.61
α_{radio}	0.72	0.74	0.73
q_{IR}	0.37	0.31	0.34
$\log \lambda_{\text{Edd}}$	-1.95	-0.94	-1.54

SFR of HSC-level objects is larger than that of SDSS-level objects (Sections 3.5.2 and 3.5.3).

3. Total IR luminosity and IR luminosity contributed from AGN increase with increasing redshift, and thus those luminosities of HSC-level objects are larger than those of SDSS-level objects. Most HSC-level objects are classified as ULIRGs with $\log(L_{\text{IR}}/L_\odot) > 12.0$ (Sections 3.5.4 and 3.5.5).
4. Radio spectral index (α_{radio}) and luminosity ratio of IR and radio (q_{IR}) do not significantly depend on redshift. However, the mean α_{radio} of HSC-level objects is slightly larger than that of SDSS-level objects, while mean q_{IR} of HSC-level objects is smaller than that of SDSS-level objects (Sections 3.5.6 and 3.5.7).
5. Eddington ratio (λ_{Edd}) of HSC-level objects is larger than that of SDSS-level objects, suggesting that optically faint HSC-level RGs discovered by HSC and FIRST could be dust-obscured AGNs with actively growing SMBHs (Section 4.6).

Overall, our HSC–FIRST sample seems to have a variety of RGs, including classical ones with massive host, low SFR, and low Eddington ratio, and a sort of new population with less massive host, high SFR, and high Eddington ratio. In particular, the later ones are optically faint and high redshift RGs that cannot be discovered by the SDSS, whose properties differ from a classical view of RGs. We conclude that the WERGS project with HSC and FIRST explores a new population that would be missed by previous surveys.

We gratefully acknowledge the anonymous referee for a careful reading of the manuscript and very helpful comments. We are deeply thankful to Prof. Denis Burgarella, Dr. Meric Boquien, and Dr. Laure Ciesla for helping us to understand CIGALE code.

The Hyper Suprime-Cam (HSC) collaboration includes the astronomical communities of Japan and Taiwan, and Princeton University. The HSC instrumentation and software were developed by the National Astronomical Observatory of Japan (NAOJ), the Kavli Institute for the Physics and Mathematics of the Universe (Kavli IPMU), the University of Tokyo, the High Energy Accelerator Research Organization (KEK), the Academia Sinica Institute for Astronomy and Astrophysics in Taiwan (ASIAA), and Princeton University. Funding was contributed by the FIRST program from Japanese Cabinet Office, the Ministry of Education, Culture, Sports, Science and Technology (MEXT), the Japan Society for the Promotion of Science (JSPS), Japan Science and Technology Agency (JST), the

Toray Science Foundation, NAOJ, Kavli IPMU, KEK, ASIAA, and Princeton University.

This paper makes use of software developed for the Large Synoptic Survey Telescope. We thank the LSST Project for making their code available as free software at <http://dm.lsstcorp.org>.

The Pan-STARRS1 Surveys (PS1) have been made possible through contributions of the Institute for Astronomy, the University of Hawaii, the Pan-STARRS Project Office, the Max Planck Society and its participating institutes, the Max Planck Institute for Astronomy, Heidelberg and the Max Planck Institute for Extraterrestrial Physics, Garching, the Johns Hopkins University, Durham University, the University of Edinburgh, Queen's University Belfast, the Harvard-Smithsonian Center for Astrophysics, the Las Cumbres Observatory Global Telescope Network Incorporated, the National Central University of Taiwan, the Space Telescope Science Institute, the National Aeronautics and Space Administration under grant No. NNX08AR22G issued through the Planetary Science Division of the NASA Science Mission Directorate, the National Science Foundation under grant No. AST-1238877, the University of Maryland, and Eotvos Lorand University (ELTE).

Based on data collected at the Subaru Telescope and retrieved from the HSC data archive system, which is operated by Subaru Telescope and Astronomy Data Center at National Astronomical Observatory of Japan.

The National Radio Astronomy Observatory is a facility of the National Science Foundation operated under cooperative agreement by Associated Universities, Inc.

Based on data products from observations made with ESO Telescopes at the La Silla Paranal Observatory under programme IDs 177.A-3016, 177.A-3017 and 177.A-3018, and on data products produced by Target/OmegaCEN, INAF-OACN, INAF-OAPD, and the KiDS production team, on behalf of the KiDS consortium. OmegaCEN and the KiDS production team acknowledge support by NOVA and NWO-M grants. Members of INAF-OAPD and INAF-OACN also acknowledge the support from the Department of Physics & Astronomy of the University of Padova, and of the Department of Physics of Univ. Federico II (Naples).

This publication has made use of data from the VIKING survey from VISTA at the ESO Paranal Observatory, programme ID 179.A-2004. Data processing has been contributed by the VISTA Data Flow System at CASU, Cambridge, and WFAU, Edinburgh.

The *Herschel*-ATLAS is a project with *Herschel*, which is an ESA space observatory with science instruments provided by European-led Principal Investigator consortia and with important participation from NASA. The H-ATLAS website is <http://www.h-atlas.org/>.

We thank the staff of the GMRT who made these observations possible. GMRT is run by the National Centre for Radio Astrophysics of the Tata Institute of Fundamental Research.

This research has made use of the NASA/ IPAC Infrared Science Archive, which is operated by the Jet Propulsion

Laboratory, California Institute of Technology, under contract with the National Aeronautics and Space Administration.

Funding for SDSS-III has been provided by the Alfred P. Sloan Foundation, the Participating Institutions, the National Science Foundation, and the U.S. Department of Energy Office of Science. The SDSS-III website is <http://www.sdss3.org/>. SDSS-III is managed by the Astrophysical Research Consortium for the Participating Institutions of the SDSS-III Collaboration, including the University of Arizona, the Brazilian Participation Group, Brookhaven National Laboratory, Carnegie Mellon University, University of Florida, the French Participation Group, the German Participation Group, Harvard University, the Instituto de Astrofísica de Canarias, the Michigan State/Notre Dame/JINA Participation Group, the Johns Hopkins University, Lawrence Berkeley National Laboratory, Max Planck Institute for Astrophysics, Max Planck Institute for Extraterrestrial Physics, New Mexico State University, New York University, Ohio State University, Pennsylvania State University, University of Portsmouth, Princeton University, the Spanish Participation Group, University of Tokyo, University of Utah, Vanderbilt University, University of Virginia, University of Washington, and Yale University.

GAMA is a joint European-Australasian project based around a spectroscopic campaign using the Anglo-Australian Telescope. The GAMA input catalog is based on data taken from the Sloan Digital Sky Survey and the UKIRT Infrared Deep Sky Survey. Complementary imaging of the GAMA regions is being obtained by a number of independent survey programmes including *GALEX* MIS, VST KiDS, VISTA VIKING, *WISE*, *Herschel*-ATLAS, GMRT, and ASKAP providing UV to radio coverage. GAMA is funded by the STFC (UK), the ARC (Australia), the AAO, and the participating institutions. The GAMA website is <http://www.gama-survey.org/>.

Y.T. and W.H.W. acknowledge the support from the Ministry of Science and Technology of Taiwan (*MOST* 105-2112-M-001-029-MY3). K.I. is supported by Program for Establishing a Consortium for the Development of Human Resources in Science and Technology, Japan Science and Technology Agency (JST). This work is supported by JSPS KAKENHI grant Nos. 18J01050 and 19K14759 (Y.T.), 16H01101, 16H03958, and 17H01114 (T.N.), and 18K13584 (K.I.), and 17K05384 (Y.U.).

Numerical computations/simulations were carried out (in part) using the SuMIRe cluster operated by the Extragalactic OIR group at ASIAA.

Facilities: Subaru (HSC), ESO:VISTA, *WISE*, *Herschel*, VLA, GMRT, IRSA.

Software: IDL, IDL Astronomy User's Library (Landsman 1993), TOPCAT (Taylor 2006), CIGALE (Boquien et al. 2019).

Appendix A HSC–FIRST Radio Galaxy Catalog

We provide HSC–FIRST RG catalog that includes 1056 RGs used for the SED fitting with CIGALE. The catalog description is summarized in Table 3.

Table 3
Format and Column Descriptions of HSC–FIRST RG Catalog

Column name	Format	Unit	Description
ID	LONG		Unique id
Name	STRING		Object name in the FIRST catalog
R.A.	DOUBLE	degree	Right ascension (J2000.0) from HSC S16a wide catalog
Decl.	DOUBLE	degree	Decl. (J2000.0) from HSC S16a wide catalog
Redshift	DOUBLE		Redshift
Ref_redshift	STRING		Reference of redshift (mizuki/SDSS DR12/GAMA DR2/WIGGLEZ-DR1)
<i>u</i> mag	DOUBLE	AB mag.	<i>u</i> -band magnitude from KiDS DR3
<i>u</i> mag_err	DOUBLE	AB mag.	<i>u</i> -band magnitude error from KiDS DR3
<i>g</i> mag	DOUBLE	AB mag.	<i>g</i> -band magnitude from HSC S16a wide catalog
<i>g</i> mag_err	DOUBLE	AB mag.	<i>g</i> -band magnitude error from HSC S16a wide catalog
<i>r</i> mag	DOUBLE	AB mag.	<i>r</i> -band magnitude from HSC S16a wide catalog
<i>r</i> mag_err	DOUBLE	AB mag.	<i>r</i> -band magnitude error from HSC S16a wide catalog
<i>i</i> mag	DOUBLE	AB mag.	<i>i</i> -band magnitude from HSC S16a wide catalog
<i>i</i> mag_err	DOUBLE	AB mag.	<i>i</i> -band magnitude error from HSC S16a wide catalog
<i>z</i> mag	DOUBLE	AB mag.	<i>z</i> -band magnitude from HSC S16a wide catalog
<i>z</i> mag_err	DOUBLE	AB mag.	<i>z</i> -band magnitude error from HSC S16a wide catalog
<i>y</i> mag	DOUBLE	AB mag.	<i>y</i> -band magnitude from HSC S16a wide catalog
<i>y</i> mag_err	DOUBLE	AB mag.	<i>y</i> -band magnitude error from HSC S16a wide catalog
<i>J</i> mag	DOUBLE	AB mag.	<i>J</i> -band magnitude from VIKING DR3
<i>J</i> mag_err	DOUBLE	AB mag.	<i>J</i> -band magnitude error from VIKING DR3
<i>H</i> mag	DOUBLE	AB mag.	<i>H</i> -band magnitude from VIKING DR3
<i>H</i> mag_err	DOUBLE	AB mag.	<i>H</i> -band magnitude error from VIKING DR3
<i>Ks</i> mag	DOUBLE	AB mag.	<i>Ks</i> -band magnitude from VIKING DR3
<i>Ks</i> mag_err	DOUBLE	AB mag.	<i>Ks</i> -band magnitude error from VIKING DR3
w1mag	DOUBLE	Vega mag	3.4 μ m magnitude from ALLWISE
w1mag_err	DOUBLE	Vega mag	3.4 μ m magnitude error from ALLWISE
w2mag	DOUBLE	Vega mag	4.6 μ m magnitude from ALLWISE
w2mag_err	DOUBLE	Vega mag	4.6 μ m magnitude error from ALLWISE
w3mag	DOUBLE	Vega mag	12 μ m magnitude from ALLWISE
w3mag_err	DOUBLE	Vega mag	12 μ m magnitude error from ALLWISE
w4mag	DOUBLE	Vega mag	22 μ m magnitude from ALLWISE
w4mag_err	DOUBLE	Vega mag	22 μ m magnitude error from ALLWISE
A_u	DOUBLE	mag	Galactic extinction correction for <i>u</i> -band
A_g	DOUBLE	mag	Galactic extinction correction for <i>g</i> -band
A_r	DOUBLE	mag	Galactic extinction correction for <i>r</i> -band
A_i	DOUBLE	mag	Galactic extinction correction for <i>i</i> -band
A_z	DOUBLE	mag	Galactic extinction correction for <i>z</i> -band
A_y	DOUBLE	mag	Galactic extinction correction for <i>y</i> -band
A_j	DOUBLE	mag	Galactic extinction correction for <i>J</i> -band
A_h	DOUBLE	mag	Galactic extinction correction for <i>H</i> -band
A_ks	DOUBLE	mag	Galactic extinction correction for <i>Ks</i> -band
Flux_34	DOUBLE	mJy	Flux density at 3.4 μ m
Flux_34_err	DOUBLE	mJy	Uncertainty of flux density at 3.4 μ m
Flux_46	DOUBLE	mJy	Flux density at 4.6 μ m
Flux_46_err	DOUBLE	mJy	Uncertainty of flux density at 4.6 μ m
Flux_12	DOUBLE	mJy	Flux density at 12 μ m
Flux_12_err	DOUBLE	mJy	Uncertainty of flux density at 12 μ m
Flux_22	DOUBLE	mJy	Flux density at 22 μ m flux density
Flux_22_err	DOUBLE	mJy	Uncertainty of flux density at 22 μ m
Flux_100	DOUBLE	mJy	Flux density at 100 μ m from H-ATLAS DR1
Flux_100_err	DOUBLE	mJy	Uncertainty of flux density at 100 μ m from H-ATLAS DR1
Flux_160	DOUBLE	mJy	Flux density at 160 μ m from H-ATLAS DR1
Flux_160_err	DOUBLE	mJy	Uncertainty of flux density at 160 μ m from H-ATLAS DR1
Flux_250	DOUBLE	mJy	Flux density at 250 μ m from H-ATLAS DR1
Flux_250_err	DOUBLE	mJy	Uncertainty of flux density at 250 μ m from H-ATLAS DR1
Flux_350	DOUBLE	mJy	Flux density at 350 μ m from H-ATLAS DR1
Flux_350_err	DOUBLE	mJy	Uncertainty of flux density at 350 μ m from H-ATLAS DR1
Flux_500	DOUBLE	mJy	Flux density at 500 μ m from H-ATLAS DR1
Flux_500_err	DOUBLE	mJy	Uncertainty of flux density at 500 μ m from H-ATLAS DR1
Flux_14G	DOUBLE	mJy	Flux density at 1.4 GHz from FIRST
Flux_14G_err	DOUBLE	mJy	Uncertainty pf flux density at 1.4 GHz from FIRST
Flux_150M	DOUBLE	mJy	Flux density at 150 MHz from TGSS ADR1
Flux_150M_err	DOUBLE	mJy	Uncertainty pf flux density at 150 MHz from TGSS ADR1

Table 3
(Continued)

Column name	Format	Unit	Description
Flag_u	INT		Flag for u -band data (0: CIGALE. 1: CIGALE with 3σ upper limit, 2: non CIGALE)
Flag_g	INT		Flag for g -band data (0: CIGALE. 1: CIGALE with 3σ upper limit, 2: non CIGALE)
Flag_r	INT		Flag for r -band data (0: CIGALE. 1: CIGALE with 3σ upper limit, 2: non CIGALE)
Flag_i	INT		Flag for i -band data (0: CIGALE. 1: CIGALE with 3σ upper limit, 2: non CIGALE)
Flag_z	INT		Flag for z -band data (0: CIGALE. 1: CIGALE with 3σ upper limit, 2: non CIGALE)
Flag_y	INT		Flag for y -band data (0: CIGALE. 1: CIGALE with 3σ upper limit, 2: non CIGALE)
Flag_j	INT		Flag for j -band data (0: CIGALE. 1: CIGALE with 3σ upper limit, 2: non CIGALE)
Flag_h	INT		Flag for h -band data (0: CIGALE. 1: CIGALE with 3σ upper limit, 2: non CIGALE)
Flag_ks	INT		Flag for ks -band data (0: CIGALE. 1: CIGALE with 3σ upper limit, 2: non CIGALE)
Flag_34	INT		Flag for $3.4 \mu\text{m}$ data (0: CIGALE. 1: CIGALE with 3σ upper limit, 2: non CIGALE)
Flag_46	INT		Flag for $4.6 \mu\text{m}$ data (0: CIGALE. 1: CIGALE with 3σ upper limit, 2: non CIGALE)
Flag_12	INT		Flag for $12 \mu\text{m}$ data (0: CIGALE. 1: CIGALE with 3σ upper limit, 2: non CIGALE)
Flag_22	INT		Flag for $22 \mu\text{m}$ data (0: CIGALE. 1: CIGALE with 3σ upper limit, 2: non CIGALE)
Flag_100	INT		Flag for $100 \mu\text{m}$ data (0: CIGALE. 1: CIGALE with 3σ upper limit, 2: non CIGALE)
Flag_160	INT		Flag for $160 \mu\text{m}$ data (0: CIGALE. 1: CIGALE with 3σ upper limit, 2: non CIGALE)
Flag_250	INT		Flag for $250 \mu\text{m}$ data (0: CIGALE. 1: CIGALE with 3σ upper limit, 2: non CIGALE)
Flag_350	INT		Flag for $350 \mu\text{m}$ data (0: CIGALE. 1: CIGALE with 3σ upper limit, 2: non CIGALE)
Flag_500	INT		Flag for $500 \mu\text{m}$ data (0: CIGALE. 1: CIGALE with 3σ upper limit, 2: non CIGALE)
Flag_14G	INT		Flag for 1.4 GHz data (0: CIGALE. 1: CIGALE with 3σ upper limit, 2: non CIGALE)
Flag_150M	INT		Flag for 150 MHz data (0: CIGALE. 1: CIGALE with 3σ upper limit, 2: non CIGALE)
log_L14G ^a	DOUBLE	W Hz^{-1}	Rest-frame luminosity density at 1.4 GHz
log_L14G_err	DOUBLE	W Hz^{-1}	Uncertainty of rest-frame luminosity density at 1.4 GHz
E_BV	DOUBLE		Color excess ($E(B - V)$) derived from CIGALE
E_BV_err	DOUBLE		Uncertainty of color excess ($E(B - V)$) derived from CIGALE
log_M	DOUBLE	M_{\odot}	Stellar mass derived from CIGALE
log_M_err	DOUBLE	M_{\odot}	Uncertainty of stellar mass derived from CIGALE
log_SFR	DOUBLE	$M_{\odot} \text{ yr}^{-1}$	SFR derived from CIGALE
log_SFR_err	DOUBLE	$M_{\odot} \text{ yr}^{-1}$	Uncertainty of SFR derived from CIGALE
log_SFR_IR	DOUBLE	$M_{\odot} \text{ yr}^{-1}$	SFR derived from Equation (8)
log_LIR	DOUBLE	L_{\odot}	IR luminosity derived from CIGALE
log_LIR_err	DOUBLE	L_{\odot}	Uncertainty of IR luminosity derived from CIGALE
log_LIR_AGN	DOUBLE	L_{\odot}	IR luminosity contributed from AGN derived from CIGALE
log_LIR_AGN_err	DOUBLE	L_{\odot}	Uncertainty of IR luminosity contributed from AGN derived from CIGALE
alpha_radio	DOUBLE		Radio spectral index (α_{radio}) derived from Equation (1)
alpha_radio_err	DOUBLE		Uncertainty of radio spectral index (α_{radio})
q _{IR}	DOUBLE		q_{IR} derived from Equation (4)
q _{IR_err}	DOUBLE		Uncertainty of q_{IR}
DOF	INT		Degree of freedom for the SED fitting
rechi2	DOUBLE		Reduced χ^2 derived from CIGALE
log_MBH	DOUBLE	M_{\odot}	Black hole mass derived from stellar mass
log_Lbol	DOUBLE	L_{\odot}	Bolometric luminosity derived from the best-fit SED
log_ledd	DOUBLE		Eddington ratio (λ_{Edd})

Note.

^a If an object has α_{radio} , $\log L_{1.4 \text{ GHz}}$ is derived from Equation (3). Otherwise, we assume $\alpha_{\text{radio}} = 0.7$ for a calculation (see Section 3.3).

(This table is available in its entirety in machine-readable form.)

Appendix B

Best-fit SED for Each Radio Galaxy

The best-fit SED derived by CIGALE is available in Table 4. We strongly encourage using a template of objects




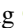

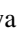
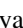

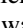

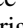


with reduced $\chi^2 < 5.0$ for science. In addition, if you use the radio part of the best-fit SED, we recommend employing the template only for objects with TGSS detections.

Table 4
Best-fit SED Template of Each HSC–FIRST RG

Column name	Format	Unit	Description
ID	LONG		Unique id
Wavelength	DOUBLE	μm	Wavelength
FNU	DOUBLE	mJy	Flux density at each wavelength
LNU	DOUBLE	W	Luminosity density at each wavelength

(This table is available in its entirety in machine-readable form.)

ORCID iDs

Yoshiki Toba  <https://orcid.org/0000-0002-3531-7863>
 Takuji Yamashita  <https://orcid.org/0000-0002-4999-9965>
 Tohru Nagao  <https://orcid.org/0000-0002-7402-5441>
 Wei-Hao Wang  <https://orcid.org/0000-0003-2588-1265>
 Yoshihiro Ueda  <https://orcid.org/0000-0001-7821-6715>
 Kohei Ichikawa  <https://orcid.org/0000-0002-4377-903X>
 Masayuki Akiyama  <https://orcid.org/0000-0002-2651-1701>
 Bau-Ching Hsieh  <https://orcid.org/0000-0001-5615-4904>
 Masaru Kajisawa  <https://orcid.org/0000-0002-1732-6387>
 Chien-Hsiu Lee  <https://orcid.org/0000-0003-1700-5740>
 Akatoki Noboriguchi  <https://orcid.org/0000-0002-5197-8944>
 Masafusa Onoue  <https://orcid.org/0000-0003-2984-6803>
 Masayuki Tanaka  <https://orcid.org/0000-0002-5011-5178>

References

- Aihara, H., AlSayyad, Y., Ando, M., et al. 2019, arXiv:1905.12221
 Aihara, H., Arimoto, N., Armstrong, R., et al. 2018a, *PASJ*, 70, S4
 Aihara, H., Armstrong, R., Bickerton, S., et al. 2018b, *PASJ*, 70, S8
 Alam, S., Albareti, F. D., Allende Prieto, C., et al. 2015, *ApJS*, 219, 12
 Aniyar, A. K., & Thorat, K. 2017, *ApJS*, 230, 20
 Arnaboldi, M., Neeser, M. J., Parker, L. C., et al. 2007, *Msngr*, 127, 28
 Banfield, J. K., Wong, O. I., Willett, K. W., et al. 2015, *MNRAS*, 453, 2326
 Becker, R. H., White, R. L., & Helfand, D. J. 1995, *ApJ*, 450, 559
 Bell, E. F. 2003, *ApJ*, 586, 794
 Best, P. N., & Heckman, T. M. 2012, *MNRAS*, 421, 1569
 Best, P. N., Kauffmann, G., Heckman, T. M., & Ivezić, Ž. 2005, *MNRAS*, 362, 9
 Blundell, K. M., Rawlings, S., & Willott, C. J. 1999, *AJ*, 117, 677
 Bonzini, M., Mainieri, V., Padovani, P., et al. 2015, *MNRAS*, 453, 1079
 Boquien, M., Burgarella, D., Roehlich, Y., et al. 2019, *A&A*, 622, A103
 Bornancini, C. G., O’Mill, A. L., Gurovich, S., & Lambas, D. G. 2010, *MNRAS*, 406, 197
 Bosch, J., Armstrong, R., Bickerton, S., et al. 2018, *PASJ*, 70, S5
 Bourne, N., Dunne, L., Maddox, S. J., et al. 2016, *MNRAS*, 462, 1714
 Brinchmann, J., Charlot, S., White, S. D. M., et al. 2004, *MNRAS*, 351, 1151
 Bruzual, G., & Charlot, S. 2003, *MNRAS*, 344, 1000
 Burgarella, D., Buat, V., & Iglesias-Páramo, J. 2005, *MNRAS*, 360, 1413
 Buttiglione, S., Capetti, A., Celotti, A., et al. 2010, *A&A*, 509, A6
 Calistro Rivera, G., Williams, W. L., Hardcastle, M. J., et al. 2017, *MNRAS*, 469, 3468
 Calzetti, D., Armus, L., Bohlin, R. C., et al. 2000, *ApJ*, 533, 682
 Calzetti, D., Kinney, A. L., & Storchi-Bergmann, T. 1994, *ApJ*, 429, 582
 Capetti, A., Massaro, F., & Baldi, R. D. 2017a, *A&A*, 598, A49
 Capetti, A., Massaro, F., & Baldi, R. D. 2017b, *A&A*, 601, A81
 Cappellari, M., & Emsellem, E. 2004, *PASP*, 116, 138
 Casey, C. M., Chapman, S. C., Beswick, R. J., et al. 2009, *MNRAS*, 399, 121
 Chabrier, G. 2003, *PASP*, 115, 763
 Chapman, S. C., Ivison, R. J., Roseboom, I. G., et al. 2010, *MNRAS*, 409, L13
 Chen, X., Akiyama, M., Noda, H., et al. 2019, *PASJ*, 71, 29
 Chen, Y.-M., Kauffmann, G., Tremonti, C. A., et al. 2012, *MNRAS*, 421, 314
 Ching, J. H. Y., Croom, S. M., Sadler, E. M., et al. 2017, *MNRAS*, 469, 4584
 Ciesla, L., Boselli, A., Elbaz, D., et al. 2016, *A&A*, 585, A43
 Ciesla, L., Charmandaris, V., Georgakakis, A., et al. 2015, *A&A*, 576, A10
 Condon, J. J. 1989, *ApJ*, 338, 13
 Condon, J. J. 1992, *ARA&A*, 30, 575
 Coupon, J., Czakon, N., Bosch, J., et al. 2018, *PASJ*, 70, S7
 Croton, D. J., Springel, V., White, S. D. M., et al. 2006, *MNRAS*, 365, 11
 Cutri, R. M., Wright, E. L., Conrow, T., et al. 2014, *yCat*, 2328, 0
 Daddi, E., Dickinson, M., Morrison, G., et al. 2007, *ApJ*, 670, 156
 Dale, D. A., Helou, G., Magdis, G. E., et al. 2014, *ApJ*, 784, 83
 Dalton, G. B., Caldwell, M., Ward, A. K., et al. 2006, *Proc. SPIE*, 6269, 62690X
 de Gasperin, F., Intema, H. T., & Frail, D. A. 2018, *MNRAS*, 474, 5008
 de Jong, J. T. A., Verdoes Kleijn, G. A., Boxhoorn, D. R., et al. 2015, *A&A*, 582, A62
 de Jong, J. T. A., Verdoes Kleijn, G. A., Kuijken, K. H., & Valentijn, E. A. 2013, *ExA*, 35, 25
 de Jong, J. T. A., Verdoes Kleijn, G. A., Erben, T., et al. 2017, *A&A*, 604, 134
 de Ruitter, H. R., Parma, P., Fanti, R., & Fanti, C. 2015, *A&A*, 581, A33
 Del Moro, A., Alexander, D. M., Mullaney, J. R., et al. 2013, *A&A*, 549, A59
 Delvecchio, I., Smolčić, V., Zamorani, G., et al. 2017, *A&A*, 602, A3
 Delvecchio, I., Smolčić, V., Zamorani, G., et al. 2018, *MNRAS*, 481, 4971
 Domínguez, A., Siana, B., Henry, A. L., et al. 2013, *ApJ*, 763, 145
 Drinkwater, M. J., Jurek, R. J., Blake, C., et al. 2010, *MNRAS*, 401, 1429
 Driver, S. P., Hill, D. T., Kelvin, L. S., et al. 2011, *MNRAS*, 413, 971
 Drouart, G., De Breuck, C., Vernet, J., et al. 2014, *A&A*, 566, A53
 Eales, S., Dunne, L., Clements, D., et al. 2010, *PASP*, 122, 499
 Elbaz, D., Daddi, E., Le Borgne, D., et al. 2007, *A&A*, 468, 33
 Fabian, A. C. 2012, *ARA&A*, 50, 455
 Falkendal, T., De Breuck, C., Lehnert, M. D., et al. 2019, *A&A*, 621, A27
 Fanaroff, B. L., & Riley, J. M. 1974, *MNRAS*, 167, 31
 Fritz, J., Franceschini, A., & Hatziminaoglou, E. 2006, *MNRAS*, 366, 767
 Furusawa, H., Koike, M., Takata, T., et al. 2018, *PASJ*, 70, S3
 Goulding, A. D., Forman, W. R., Hickox, R. C., et al. 2014, *ApJ*, 783, 40
 Griffin, M. J., Abergel, A., Abreu, A., et al. 2010, *A&A*, 518, L3
 Gürkan, G., Hardcastle, M. J., & Jarvis, M. J. 2014, *MNRAS*, 438, 1149
 Gürkan, G., Hardcastle, M. J., Jarvis, M. J., et al. 2015, *MNRAS*, 452, 3776
 Gürkan, G., Hardcastle, M. J., Smith, D. J. B., et al. 2018, *MNRAS*, 475, 3010
 Helfand, D. J., White, R. L., & Becker, R. H. 2015, *ApJ*, 801, 26
 Helou, G., Soifer, B. T., & Rowan-Robinson, M. 1985, *ApJL*, 298, L7
 Huang, S., Leauthaud, A., Murata, R., et al. 2018, *PASJ*, 70, S6
 Ichikawa, K., Ricci, C., Ueda, Y., et al. 2017, *ApJ*, 835, 74
 Inoue, A. K. 2011, *MNRAS*, 415, 2920
 Intema, H. T., Jagannathan, P., Mooley, K. P., & Frail, D. A. 2017, *A&A*, 598, A78
 Ivezić, Ž., Menou, K., Knapp, G. R., et al. 2002, *AJ*, 124, 2364
 Ivison, R. J., Magnelli, B., Ibar, E., et al. 2010, *A&A*, 518, L31
 Janssen, R. M. J., Röttgering, H. J. A., Best, P. N., & Brinchmann, J. 2012, *A&A*, 541, A62
 Kajisawa, M., Ichikawa, T., Tanaka, I., et al. 2009, *ApJ*, 702, 1393
 Kawanomoto, S., Uruguchi, F., Komiyama, Y., et al. 2018, *PASJ*, 70, 66
 Kennicutt, R. C., Jr. 1998, *ARA&A*, 36, 189
 Kewley, L. J., Geller, M. J., & Jansen, R. A. 2004, *AJ*, 127, 2002
 Komiyama, Y., Obuchi, Y., Nakaya, H., et al. 2018, *PASJ*, 70, S2
 Kroupa, P. 2001, *MNRAS*, 322, 231
 Kuijken, K. 2011, *Msngr*, 146, 8
 Laigle, C., McCracken, H. J., Ilbert, O., et al. 2016, *ApJS*, 224, 24
 Laing, R. A. 1994, in ASP Conf. Ser. 54, The Physics of Active Galaxies 227, ed. G. V. Bicknell, M. A. Dopita, & P. J. Quinn (San Francisco, CA: ASP)
 Landsman, W. B. 1993, in ASP Conf. Ser. 52, Astronomical Data Analysis Software and Systems II, ed. R. J. Hanisch, R. J. V. Brissenden, & J. Barnes (San Francisco, CA: ASP), 246
 Lee, N., Sanders, D. B., Casey, C. M., et al. 2015, *ApJ*, 801, 80
 Liske, J., Baldry, I. K., Driver, S. P., et al. 2015, *MNRAS*, 452, 2087
 Lukic, V., Brüggem, M., Banfield, J. K., et al. 2018, *MNRAS*, 476, 246
 Lyu, J., & Rieke, G. H. 2018, *ApJ*, 866, 92
 Maddox, N. 2018, *MNRAS*, 480, 5203
 Magnelli, B., Lutz, D., Berta, S., et al. 2010, *A&A*, 518, L28
 Maraston, C., Pforr, J., Renzini, A., et al. 2010, *MNRAS*, 407, 830
 Maraston, C., & Strömbäck, G. 2011, *MNRAS*, 418, 2785
 Martini, P., Dicken, D., & Storchi-Bergmann, T. 2013, *ApJ*, 766, 121
 Mason, R. E., Lopez-Rodriguez, E., Packham, C., et al. 2012, *AJ*, 144, 11
 Mateos, S., Alonso-Herrero, A., Carrera, F. J., et al. 2012, *MNRAS*, 426, 3271
 Mateos, S., Alonso-Herrero, A., Carrera, F. J., et al. 2013, *MNRAS*, 434, 941
 Matsuoka, K., Toba, Y., Shidatsu, M., et al. 2018, *A&A*, 620, L3
 McLure, R. J., Jarvis, M. J., Targett, T. A., Dunlop, J. S., & Best, P. N. 2006, *MNRAS*, 368, 1395
 Mingo, B., Watson, M. G., Rosen, S. R., et al. 2016, *MNRAS*, 462, 2631

- Miyazaki, S., Komiyama, Y., Kawanomoto, S., et al. 2018, *PASJ*, 70, S1
- Miyazaki, S., Komiyama, Y., Nakaya, H., et al. 2012, *Proc. SPIE*, 8446, 84460Z
- Morganti, R., Fogasy, J., Paragi, Z., Oosterloo, T., & Orienti, M. 2013, *Sci*, 341, 1082
- Netzer, H. 2009, *MNRAS*, 399, 1907
- Noboriguchi, A., Nagao, T., Toba, Y., et al. 2019, *ApJ*, 876, 132
- Noll, S., Burgarella, D., Giovannoli, E., et al. 2009, *A&A*, 507, 3
- Padovani, P. 2016, *A&ARv*, 24, 13
- Pearson, W. J., Wang, L., Hurley, P. D., et al. 2018, *A&A*, 615, A146
- Pe'er, A. 2014, *SSRv*, 183, 371
- Petrosian, V. 1976, *ApJL*, 209, L1
- Pilbratt, G. L., Riedinger, J. R., Passvogel, T., et al. 2010, *A&A*, 518, L1
- Poglitich, A., Waelkens, C., Geis, N., et al. 2010, *A&A*, 518, L2
- Prescott, M., Whittam, I. H., Jarvis, M. J., et al. 2018, *MNRAS*, 480, 707
- Privon, G. C., Baum, S. A., O'Dea, C. P., et al. 2012, *ApJ*, 747, 46
- Rakshit, S., Johnson, A., Stalin, C. S., Gandhi, P., Hoenig, S., et al. 2019, *MNRAS*, 483, 2362
- Read, S. C., Smith, D. J. B., Gürkan, G., et al. 2018, *MNRAS*, 480, 5625
- Reines, A. E., & Volonteri, M. 2015, *ApJ*, 813, 82
- Rocca-Volmerange, B., Le Borgne, D., De Breuck, C., Fioc, M., & Moy, E. 2004, *A&A*, 415, 931
- Rosario, D. J., Santini, P., Lutz, D., et al. 2012, *A&A*, 545, A45
- Sajina, A., Yan, L., Lutz, D., et al. 2008, *ApJ*, 683, 659
- Salim, S., Lee, J. C., Janowiecki, S., et al. 2016, *ApJS*, 227, 2
- Salim, S., Rich, R. M., Charlot, S., et al. 2007, *ApJS*, 173, 267
- Salpeter, E. E. 1955, *ApJ*, 121, 161
- Sanders, D. B., & Mirabel, I. F. 1996, *ARA&A*, 34, 749
- Sarzi, M., Falcón-Barroso, J., Davies, R. L., et al. 2006, *MNRAS*, 366, 1151
- Sawicki, M. 2012, *PASP*, 124, 1208
- Schlegel, D. J., Finkbeiner, D. P., & Davis, M. 1998, *ApJ*, 500, 525
- Seymour, N., Altieri, B., De Breuck, C., et al. 2012, *ApJ*, 755, 146
- Seymour, N., Stern, D., De Breuck, C., et al. 2007, *ApJS*, 171, 353
- Shao, L., Lutz, D., Nordon, R., et al. 2010, *A&A*, 518, L26
- Singh, V., & Chand, H. 2018, *MNRAS*, 480, 1796
- Singh, V., Ishwara-Chandra, C. H., Wadadekar, Y., Beelen, A., & Kharb, P. 2015, *MNRAS*, 446, 599
- Smolčić, V. 2009, *ApJL*, 699, L43
- Smolčić, V., Delvecchio, I., Zamorani, G., et al. 2017a, *A&A*, 602, A2
- Smolčić, V., Novak, M., Bondi, M., et al. 2017b, *A&A*, 602, A1
- Speagle, J. S., Steinhardt, C. L., Capak, P. L., & Silverman, J. D. 2014, *ApJS*, 214, 15
- Stanley, F., Alexander, D. M., Harrison, C. M., et al. 2017, *MNRAS*, 472, 2221
- Swarup, G. 1991, in ASP Conf. Ser. 19, Radio Interferometry: Theory, Techniques, and Applications, ed. T. J. Cornwell & R. A. Perley (San Francisco, CA: ASP), 376
- Tanaka, M. 2015, *ApJ*, 801, 20
- Tanaka, M., Coupon, J., Hsieh, B.-C., et al. 2018, *PASJ*, 70, S9
- Taylor, M. B. 2006, in ASP Conf. Ser. 351, Astronomical Data Analysis Software and Systems XV, ed. C. Gabriel et al. (San Francisco, CA: ASP), 666
- Thomas, D., Maraston, C., & Johansson, J. 2011, *MNRAS*, 412, 2183
- Toba, Y., Bae, H.-J., Nagao, T., et al. 2017a, *ApJ*, 850, 140
- Toba, Y., & Nagao, T. 2016, *ApJ*, 820, 46
- Toba, Y., Nagao, T., Kajisawa, M., et al. 2017b, *ApJ*, 835, 36
- Toba, Y., Nagao, T., Strauss, M. A., et al. 2015, *PASJ*, 67, 86
- Toba, Y., Nagao, T., Wang, W.-H., et al. 2017c, *ApJ*, 840, 21
- Toba, Y., Oyabu, S., Matsuhara, H., et al. 2014, *ApJ*, 788, 45
- Toba, Y., Ueda, J., Lim, C.-F., et al. 2018, *ApJ*, 857, 31
- Toba, Y., Ueda, Y., Matsuoka, K., et al. 2019, *MNRAS*, 484, 196
- Tomczak, A. R., Quadri, R. F., Tran, K.-V. H., et al. 2016, *ApJ*, 817, 118
- Ueda, Y., Hatsukade, B., Kohno, K., et al. 2018, *ApJ*, 853, 24
- Valiante, E., Smith, M. W. L., Eales, S., et al. 2016, *MNRAS*, 462, 3146
- White, R. L., Becker, R. H., Helfand, D. J., & Gregg, M. D. 1997, *ApJ*, 475, 479
- Whittam, I. H., Prescott, M., McAlpine, K., Jarvis, M. J., & Heywood, I. 2018, *MNRAS*, 480, 358
- Williams, W. L., Calistro Rivera, G., Best, P. N., et al. 2018, *MNRAS*, 475, 3429
- Wright, E. L., Eisenhardt, P. R. M., Mainzer, A. K., et al. 2010, *AJ*, 140, 1868
- Yamashita, T., Nagao, T., Akiyama, M., et al. 2018, *ApJ*, 866, 140 (Paper I)
- Yang, X.-h., Chen, P.-s., & Huang, Y. 2015, *MNRAS*, 449, 3191
- York, D. G., Adelman, J., Anderson, J. E., Jr., et al. 2000, *AJ*, 120, 1579
- Yun, M. S., Reddy, N. A., Condon, J. J., et al. 2001, *ApJ*, 554, 803